The Astrophysical Journal, 985:82 (28pp), 2025 May 20 https://doi.org/10.3847/1538-4357/adc4e3

© 2025. The Author(s). Published by the American Astronomical Society.

OPEN ACCESS

Physics-based Simulation of the 2013 April 11 Solar Energetic Particle Event

Weihao Liu[1], Igor V. Sokolov[1], Lulu Zhao[1], Tamas I. Gombosi[1], Nishtha Sachdeva[1], Xiaohang Chen[1], Gábor Tóth[1], David Lario[2], Ward B. Manchester, IV[1], Kathryn Whitman[3,4], Christina M. S. Cohen[5], Alessandro Bruno[2,6], M. Leila Mays[2], and Hazel M. Bain[7,8]

[1] Department of Climate and Space Sciences and Engineering, University of Michigan, Ann Arbor, MI 48109, USA; whliu@umich.edu
[2] Heliophysics Science Division, NASA Goddard Space Flight Center, Greenbelt, MD 20771, USA
[3] Space Radiation Analysis Group, NASA Johnson Space Center, Houston, TX 77058, USA
[4] KBR, Houston, TX 77002, USA
[5] California Institute of Technology, Pasadena, CA 91125, USA
[6] Department of Physics, Catholic University, Washington, DC 20064, USA
[7] Cooperative Institute for Research in Environmental Sciences, University of Colorado Boulder, Boulder, CO 80309, USA
[8] NOAA Space Weather Prediction Center, Boulder, CO 80305, USA

Received 2025 January 28; revised 2025 March 21; accepted 2025 March 23; published 2025 May 15

Abstract

Solar energetic particles (SEPs) can pose hazardous radiation risks to both humans and spacecraft electronics in space. Numerical modeling based on first principles offers valuable insights into the underlying physics of SEPs and provides synthetic observables for SEPs at any time and location in the inner heliosphere. In this work, we present a numerical scheme, which conserves the number of particles based on integral relations for Poisson brackets, to solve the kinetic equation for particle acceleration and transport processes. We implement this scheme within the Space Weather Modeling Framework, developed at the University of Michigan. In addition, we develop a new shock-capturing tool to study the coronal mass ejection-driven shock originating from the low solar corona. These methodological advancements are applied to conduct a comprehensive study of a historical SEP event on 2013 April 11. Observations from multiple spacecraft, including the Solar and Heliospheric Observatory, Solar Dynamics Observatory, Geostationary Operational Environmental Satellite, Advanced Composition Explorer near Earth, and STEREO-A/B, are used for model–data comparison and validation. We show synthetic observables, including extreme ultraviolet and white-light images, proton time–intensity profiles, and energy spectra, and discuss their differences and probable explanations compared to observations. Our simulation results demonstrate the application of the Poisson bracket scheme with a particle solver to simulating a historical SEP event. We also show the capability of extracting the complex shock surface using our shock-capturing tool and understand how the complex shock surface affects the particle acceleration process.

Unified Astronomy Thesaurus concepts: Solar energetic particles (1491); Solar coronal mass ejection shocks (1997); Heliosphere (711); Space weather (2037); Computational methods (1965)

1. Introduction

Solar energetic particles (SEPs) consist of protons, heavier ions, and electrons originating in association with solar eruptions. They are observed at energies ranging from suprathermal (a few keV per nucleon) to relativistic (a few GeV per nucleon) (D. V. Reames 1999, 2021; K.-L. Klein & S. Dalla 2017). Generally, SEP events can be classified into impulsive or gradual ones (H. Cane et al. 2006; D. V. Reames 2013). Impulsive SEP events are believed to be associated with magnetic reconnection processes within solar flares and coronal jets. Their time–intensity profiles usually show a sudden onset followed by a fast decay with a duration typically less than 1 day (e.g., N. V. Nitta et al. 2006; G. Mason 2007; R. Bučik 2020; D. Lario et al. 2024). On the other hand, gradual SEP events are usually associated with shocks driven by coronal mass ejections (CMEs) and typically last for a few days (S. Kahler et al. 1978, 1984; M. Desai & J. Giacalone 2016).

CMEs can drive shock waves that have been identified in coronagraph images (D. Sime & A. Hundhausen 1987; A. Vourlidas et al. 2003) and are often observed in situ at 1 astronomical unit (au) and sometimes at larger heliocentric distances up to several astronomical units (P. Chen 2011; D. F. Webb & T. A. Howard 2012; W. B. Manchester et al. 2017). As a shock wave propagates across the solar corona (SC) and through the interplanetary (IP) medium, it may continue to accelerate particles from the ambient solar wind plasma or remnants from previous events (e.g., N. Gopalswamy et al. 2002; A. Rouillard et al. 2011; J. G. Luhmann et al. 2020). The resulting energetic particles can then propagate through the SC and IP space, reaching Earth's location and posing hazardous radiation risks to both humans and spacecraft in space (e.g., L. I. Miroshnichenko 2018; J. Guo et al. 2021, 2024; N. Buzulukova & B. Tsurutani 2022; E. W. Cliver et al. 2022). Therefore, a better understanding of the acceleration and transport of SEPs and the capability to predict SEPs become critical to the human endeavor for deep space exploration.

Diffusive shock acceleration (DSA), also known as first-order Fermi acceleration (E. Fermi 1949), is believed to be the mechanism at shock fronts that produces energetic particles in many heliophysics and astrophysical systems (e.g., W. Axford et al. 1977; G. Krymskii 1977; A. Bell 1978a, 1978b; R. D. Blandford & J. P. Ostriker 1978; R. Blandford & D. Eichler 1987; J. Jokipii 1982, 1987; T. P. Armstrong et al. 1985; G. Zank et al. 2000; V. Petrosian 2012). Particles can be

Original content from this work may be used under the terms of the Creative Commons Attribution 4.0 licence. Any further distribution of this work must maintain attribution to the author(s) and the title of the work, journal citation and DOI.

accelerated as they travel across a shock front with strong plasma compressions (see Chapter 13.4.2 of T. I. Gombosi 1998, and the references therein). This acceleration process can naturally lead to a universal power-law momentum distribution $f(p) \propto p^{-\gamma}$, where f is the omnidirectional distribution function and p denotes the magnitude of the particle momentum. The power-law index γ depends only on the shock compression ratio, i.e., the ratio of the plasma downstream density to the upstream value (L. O. Drury 1983; F. C. Jones & D. C. Ellison 1991; D. Melrose & M. Pope 1993; I. V. Sokolov et al. 2006b; J. Giacalone & M. Neugebauer 2008). However, in SEP energy spectra, there is usually an exponential rollover (D. C. Ellison & R. Ramaty 1985) or a double power-law feature (D. Band et al. 1993) with the rollover/break energy depending on the ion charge-to-mass ratio (e.g., C. Cohen et al. 2005; R. Mewaldt et al. 2005; A. Tylka et al. 2005; G. Li et al. 2009; F. Yu et al. 2022). Possible explanations suggested by, e.g., G. Li & M. A. Lee (2015), L. Zhao et al. (2016, 2017), and X. Kong et al. (2019) are the finite lifetimes and sizes of the shock for particle acceleration, as well as the particle transport processes.

In order to investigate the underlying acceleration and transport mechanisms of SEPs, numerous models have been developed to study their properties. These models include empirical, machine learning, and physics-based approaches, as reviewed by K. Whitman et al. (2023). Empirical and machine learning SEP models are built upon the observational data and can offer quick predictions of SEP events. On the other hand, first-principles physics-based models consider the mechanisms that regulate the observed SEP properties and use different kinds of sophisticated computational techniques (e.g., R. B. Decker 1988; C. Ng & D. Reames 1994; C. Ng et al. 2003; I. V. Sokolov et al. 2004; J. Kóta et al. 2005; A. Aran et al. 2006; J. Luhmann et al. 2007; M. Zhang et al. 2009, 2023; W. Dröge et al. 2010; R. Strauss & H. Fichtner 2015; J. Hu et al. 2017; M. Zhang & L. Zhao 2017; D. Borovikov et al. 2018; J. A. Linker et al. 2019; N. Wijsen et al. 2019; E. Palmerio et al. 2024; L. Zhao et al. 2024). These models leverage our current understanding of particle seed population, acceleration, and transport in the SC and IP space and allow us to analyze the processes responsible for the properties associated with SEP events. Due to the dimensionality and stiffness of SEP simulations, it is usually computationally expensive to obtain meaningful results from these physics-based models, and much attention and effort in model validation and evaluation is needed (H. M. Bain et al. 2023; Y. Zheng et al. 2024). Moreover, there are still challenges and open questions for the complete accurate modeling of SEP events as reported by A. Anastasiadis et al. (2019), such as the underlying physical mechanisms for particle acceleration (e.g., J. Giacalone 2005a, 2005b; M. A. Lee et al. 2012; O. P. Verkhoglyadova et al. 2015; B. T. Tsurutani et al. 2024), properties of the seed particle population injected into the acceleration process (e.g., G. Li et al. 2012; L.-G. Ding et al. 2015; B. Zhuang et al. 2021; N. Wijsen et al. 2023), and the interaction of energetic particles with the turbulent magnetic field in the heliosphere (e.g., J. Giacalone et al. 2000; G. Zank et al. 2014; N. E. Engelbrecht 2019; A. Shalchi 2020). In spite of high demands on computational resources and the challenges of developing techniques to deliver meaningful results, the physics-based models remain attractive in the community, since they are able to derive the shock properties and provide synthetic observables such as the time–intensity profiles and energy spectra of SEPs at any time and location of interest in the SC and inner heliosphere (IH). These synthetic observables can offer a unique insight to analyze the SEP events and interpret the underlying physics, advancing our knowledge of particle acceleration and transport processes.

Our previous study (L. Zhao et al. 2024) has demonstrated the capability of the Solar Wind with Field Lines and Energetic Particles (SOFIE) model as applied to predict historical SEP events. In this work, we advance the SOFIE model by introducing a newly developed shock-capturing tool and implementing a particle-number-conserving numerical scheme to simulate the acceleration and transport processes of SEPs. These methodological advancements have been applied to simulate a historical SEP event on 2013 April 11. The structure of the paper is as follows. In Section 2, we describe our numerical models in detail, including the magnetohydrodynamic (MHD) code to simulate the solar wind plasma, the CME flux rope model, and the new SEP model setup. In Section 3, we provide an overview of the 2013 April 11 SEP event investigated in this work. In Section 4, we show our simulation results and the model–data comparisons for this event. We also analyze the synthetic observables and provide plausible explanations for their differences compared to observations. Conclusions are summarized in Section 5.

2. Methodology

In order to simulate SEPs with a physics-based model, we need to have modules simulating the background solar wind, CME generation and propagation, and the particle acceleration and transport processes. In this study, we employ the Space Weather Modeling Framework (SWMF[9]) developed at the University of Michigan, which provides a high-performance computational capability to simulate the space weather environment from the upper solar chromosphere to the upper atmosphere of Earth and/or the outer heliosphere (G. Tóth et al. 2005, 2012; T. I. Gombosi et al. 2021). The SWMF has integrated various components that represent different physical domains of the space environment, each offering several models. Our focus here is on the SC and IH components for three-dimensional (3D) global solar wind simulations, the eruptive event (EE) generator for the CME study, and the particle acceleration and transport model for SEPs.

2.1. Background Solar Wind

The 3D global solar wind plasma is modeled by the Alfvén Wave Solar-atmosphere Model(-Realtime) (AWSoM(-R), B. van der Holst et al. 2010, 2014; R. Oran et al. 2013; I. V. Sokolov et al. 2013, 2021, 2022; T. I. Gombosi et al. 2018). The AWSoM-R is an Alfvén wave turbulence-driven and self-consistent solar atmosphere model and has been validated by comparing simulations and observations of both the in situ macroscopic properties of the solar wind and the line-of-sight (LOS) appearance of the corona observed at different wavelengths (e.g., L. Jian et al. 2015; X. Meng et al. 2015; N. Sachdeva et al. 2019, 2021, 2023; B. van der Holst et al. 2019, 2022; T. Shi et al. 2022; E. Wraback et al. 2024). In AWSoM-R, the Block-Adaptive-Tree-Solarwind-Roe-Upwind-Scheme (BATS-R-US) code plays a critical role in solving the

---

[9] https://github.com/SWMFsoftware

MHD equations that describe the plasma dynamics (K. G. Powell et al. 1999). The steady-state solar wind solution is obtained with the local time-stepping and the second-order shock-capturing scheme (G. Tóth et al. 2012; T. I. Gombosi et al. 2021). The inner boundary condition for the magnetic field is specified by solar magnetograms. In this study, we use the hourly updated synoptic magnetograms collected by the Global Oscillation Network Group of the National Solar Observatory (NSO/GONG,[10] J. Harvey et al. 1996; F. Hill 2018).

Owing to the limitations of the observation geometry, there are significant uncertainties in the radial magnetic field measurements of the polar regions (e.g., G. J. Petrie 2015; M. A. Reiss et al. 2023). In order to reduce these uncertainties and achieve better agreement of the global simulation results with observations, it is customary to modify the photospheric radial magnetic field in the polar regions (e.g., L. Nikolić 2019; I. V. Sokolov & T. I. Gombosi 2023; Z. Huang et al. 2024b). Specifically, the GONG-observed radial magnetic field, B_r^{GONG}, used as the boundary condition at the heliocentric distance of 1 solar radius ($r = 1\,R_{\mathrm{s}}$), is intensified in the weak-field regions using the following expression (Z. Huang et al. 2024b):

$$B_r|_{r=1\,R_{\mathrm{s}}} = \mathrm{sign}(B_r^{\mathrm{GONG}}) \times \min\left(3.75|B_r^{\mathrm{GONG}}|,\, |B_r^{\mathrm{GONG}}| + 5\,\mathrm{Gs}\right). \qquad (1)$$

Figure 1(a) shows the processed GONG magnetogram recorded at 06:04 UT on 2013 April 11, used as the input for AWSoM-R in the SWMF. To obtain a 3D distribution of the strapping field configuration, the potential field source surface (PFSS, M. D. Altschuler & G. Newkirk 1969; K. H. Schatten et al. 1969) model with the source surface at $r = 2.5\,R_{\mathrm{s}}$ is applied to express the intensified field as a series of spherical harmonics to the order of 180 in this study (G. Tóth et al. 2011).

In AWSoM-R, the coronal plasma is heated by the dissipation of two discrete turbulence populations that propagate parallel and antiparallel to the magnetic field (I. V. Sokolov et al. 2013, 2021; B. van der Holst et al. 2014). Using physically consistent treatments of wave reflection, dissipation, and heat partitioning between electrons and protons, AWSoM-R has been shown to simulate the SC plasma comparable to observations with three free parameters: the Poynting flux parameter for the energy input ($(S_{\mathrm{A}}/B)_{\odot}$), the correlation length for Alfvén wave dissipation ($L_{\perp}\sqrt{B}$), and the stochastic heating exponent and amplitude (h_{S}, A_{S}). Other parameters for the model setup are described by, e.g., I. V. Sokolov et al. (2013), B. van der Holst et al. (2014, 2022), and N. Sachdeva et al. (2019). The default settings for the free parameters are: $(S_{\mathrm{A}}/B)_{\odot} = 1.0\,\mathrm{MW\,m^{-2}\,T^{-1}}$, $L_{\perp}\sqrt{B} = 1.5 \times 10^5\,\mathrm{m\,T^{1/2}}$ and $(h_{\mathrm{S}},\ A_{\mathrm{S}}) = (0.21,\ 0.18)$, based on the studies of J. V. Hollweg (1986), L. Fisk & N. Schwadron (2001), B. De Pontieu et al. (2007), B. D. Chandran et al. (2011), I. V. Sokolov et al. (2013), B. van der Holst et al. (2014), and I. W. Hoppock et al. (2018). Recently, Z. Huang et al. (2024b) performed uncertainty quantification of these free parameters and found that the parameters have a strong dependence on solar cycle phases. In this simulation, the optimal Poynting flux parameter is $(S_{\mathrm{A}}/B)_{\odot} = 0.3\,\mathrm{MW\,m^{-2}\,T^{-1}}$ and the other two free parameters are set to default.

A validated background solar wind solution is essential for modeling the transport processes of energetic particles, as it provides the magnetic field configuration where particles propagate, thereby enabling the computation of the energetic particle properties observed by spacecraft at specific heliospheric locations (e.g., J. Hinterreiter et al. 2019; M. Jin et al. 2022; L. Zhao et al. 2024). Nevertheless, current numerical solutions of the ideal or resistive MHD equations have struggled to reproduce the aligned interplanetary streamlines and magnetic field lines in corotating frames (see the discussions by J. Kleimann et al. 2022 and S. Kennis et al. 2024). One of the reasons for this discrepancy is the numerical reconnection across the heliospheric current sheet (HCS): the reconnected field is directed across the HCS, while the global solar wind streams along the HCS, thus resulting in “V-shaped” magnetic field lines and significant misalignment between the magnetic field lines and plasma streamlines (e.g., M. Brchnelova et al. 2022; I. V. Sokolov et al. 2022). It is not feasible to follow the trajectory of particles in such “V-shaped” magnetic field lines, and thus streamlines are usually used instead (e.g., M. A. Young et al. 2021). Recently, I. V. Sokolov et al. (2022) have introduced the stream-aligned MHD method that “nudges” the magnetic field lines and plasma streamlines to restore their alignments. This stream-aligned AWSoM-R model has recently been validated in steady-state solar wind simulations (e.g., E. Wraback et al. 2024; L. Zhao et al. 2024; X. Liu et al. 2025). In this study, we utilize the stream-aligned AWSoM-R model to obtain a steady-state solar wind plasma for CME and SEP propagation.

In the simulation, we use a block-adaptive 3D spherical grid in the SC and a block-adaptive Cartesian cubic grid in the IH, with an overlapping buffer grid that couples the solutions from the SC over to the IH. The computational domain in the SC consists of grid blocks of 6 × 8 × 8 cells (*control volumes*). In heliocentric distance, r, the grid extends from 1.1 to $24\,R_{\mathrm{s}}$. Radial stretching is achieved using $\ln r$ as a coordinate instead of r. The smallest radial cell size is around $0.01\,R_{\mathrm{s}}$ near the Sun, to resolve the steep density and temperature gradients in the lower SC. The largest radial cell size in the SC is approximately $0.4\,R_{\mathrm{s}}$. Inside $r = 1.7\,R_{\mathrm{s}}$, the angular resolution is $\sim 1\overset{\circ}{.}4$; outside this radial range, the grid is coarsened by one level to $\sim 2\overset{\circ}{.}8$. The computational domain in the IH surrounds the spherical domain of the SC and is composed of 8 × 8 × 8 grid blocks, extending from 20 up to $500\,R_{\mathrm{s}}$. The cell size ranges from $\sim 0.3\,R_{\mathrm{s}}$ near the inner boundary to $\sim 20\,R_{\mathrm{s}}$ near the outer boundary in the IH. For both the SC and IH, the adaptive mesh refinement (AMR, see M. J. Berger & P. Colella 1989; T. I. Gombosi et al. 2003, 2004; B. van der Holst et al. 2011; G. Tóth et al. 2012, and references therein) technique is performed to resolve the HCS. The grid resolution is increased by a factor of 2 along the path of the CME to resolve the CME structures. The total number of cells is of the order of 5 million in the SC and 100 million in the IH.

2.2. Eruptive Event Generator

Within the steady-state solar wind domain, the CME flux rope is then modeled by the EE module in the SWMF, which has been extensively used and validated to model the CME initialization and propagation (e.g., W. B. Manchester et al. 2004, 2004a, 2004b, 2006, 2008, 2014a, 2014b; N. Lugaz et al. 2005a, 2005b, 2007, 2013; R. Kataoka et al. 2009; B. van der Holst et al. 2009; M. Jin et al. 2013, 2016, 2017a, 2017b;

---

[10] https://gong.nso.edu/data/magmap/

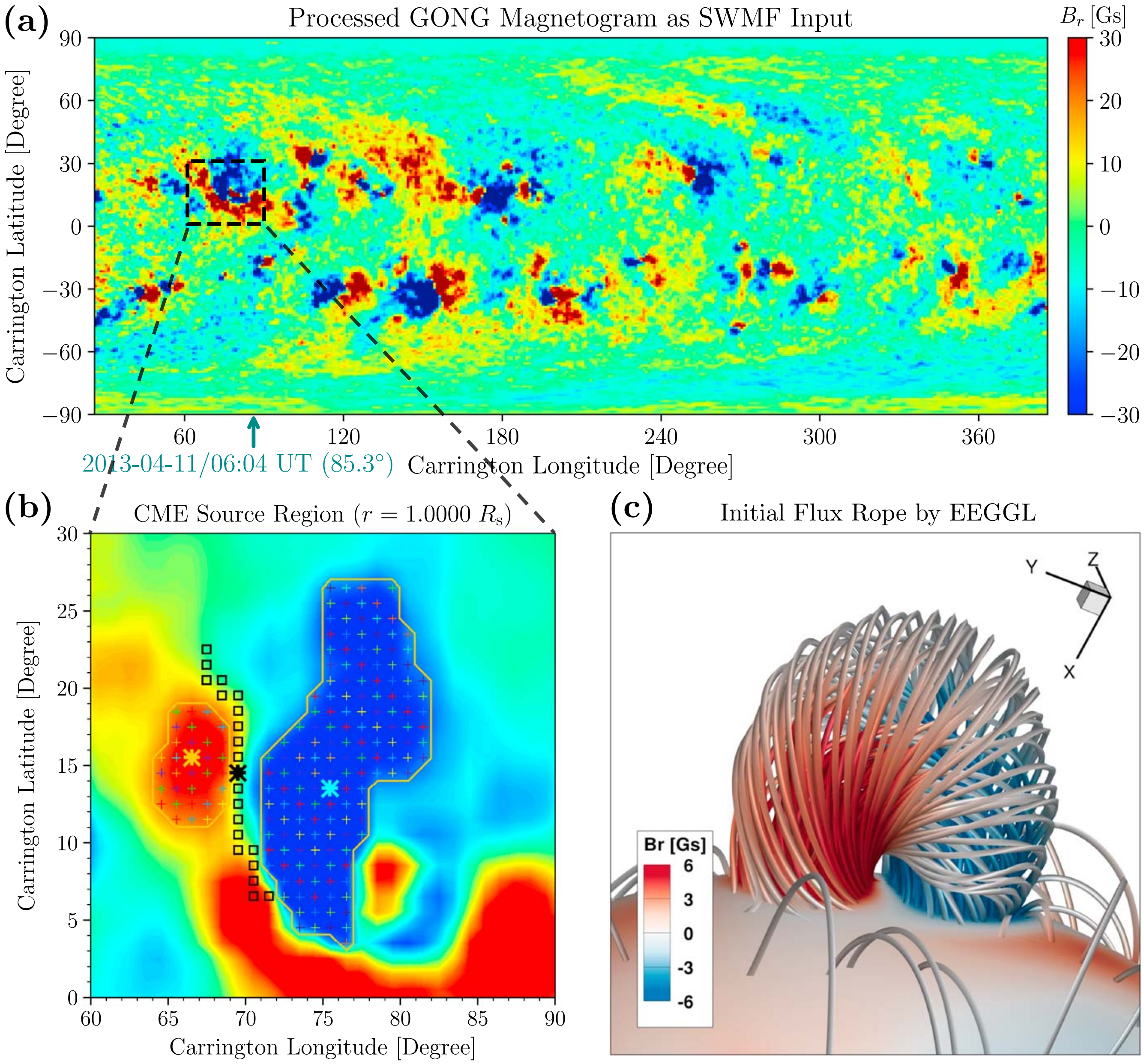

Figure 1. (a) Processed GONG magnetogram as of 06:04 UT on 2013 April 11, with the green arrow representing the Carrington longitude of Earth at that time. The magnetogram region 60° eastward of the green arrow remains unchanged from the previous Carrington rotation. Weak magnetic fields in the original GONG magnetogram have been enhanced as described by Equation (1). The black dashed box shows the area of the active region where the CME flux rope originated. (b) Zoomed-in active region field at the inner boundary, $r = 1.0000\ R_s$, with the same color bar as used in panel (a). The orange and blue asterisks indicate the chosen locations with the positive and negative magnetic polarity, respectively, and the black asterisk indicates the center of the configuration. A series of black squares denote the polarity inversion line. (c) The 3D topology of the flux rope parameterized by EEGGL, superposed with the radial magnetic field of the AR adjusted to simulate the CME event on 2013 April 11.

D. Shiota & R. Kataoka 2016; J. D. Alvarado-Gómez et al. 2018; H. Chen et al. 2025). Currently, there are a few different flux rope models embedded in the EE module, such as the breakout model (S. K. Antiochos et al. 1999), the flux-emergence model (e.g., W. B. Manchester et al. 2004), and analytical flux rope models including the Gibson—Low (GL) flux rope (S. E. Gibson & B. Low 1998), the Titov–Démoulin (TD) flux rope (V. S. Titov & P. Démoulin 1999; I. I. Roussev et al. 2003; V. S. Titov et al. 2014, 2022; I. V. Sokolov & T. I. Gombosi 2023), and the Statistical Injection of Condensed Helicity (STITCH) initialization mechanism (S. K. Antiochos 2013; J. T. Dahlin et al. 2022). The last two models can be used independently, or the STITCH model can be used to trigger the TD eruption.

In this study, we employ the spheromak-type magnetic field configuration anchored to the inner boundary, and adopt the GL model for the initial condition to erupt and propagate as a CME. For this flux rope type, the defining parameters are specified by the Eruptive Event Generator Gibson–Low (EEGGL[11]) model (e.g., S. E. Gibson & B. Low 1998; D. Borovikov et al. 2017; M. Jin et al. 2017a, 2017b). The processed GONG magnetogram shown in Figure 1(a), the location of the active region (AR), and the observed CME speed are used to calculate the GL flux rope parameters.

---

[11] Available on https://github.com/SWMFsoftware and https://ccmc.gsfc.nasa.gov/analysis/EEGGL/.

Table 1
Key Input Parameters of the AWSoM-R, EEGGL, and M-FLAMPA Models in the SWMF for This Study

Model	Parameter	Value
AWSoM-R	Poynting flux parameter ($(S_{\rm A}/B)_\odot$)	0.3 MW m^{-2} T^{-1}
	Correlation length for dissipation ($L_\perp\sqrt{B}$)	1.5×10^5 m $\mathrm{T}^{1/2}$
	Stochastic heating exponent ($h_{\rm S}$)	0.21
	Stochastic heating amplitude ($A_{\rm S}$)	0.18
EEGGL	CME speed[a]	675 km s^{-1}
	Type of the inserted flux rope	GL
	Selected AR positive pole location[b]	(66°, 16°)
	Selected AR negative pole location[b]	(75°, 14°)
	Flux rope radius	0.53 $R_{\rm s}$
	Flux rope stretching	0.60 $R_{\rm s}$
	Flux rope height	0.73 $R_{\rm s}$
	Flux rope magnetic field strength	15.0 Gs
M-FLAMPA	Diffusion coefficient free parameter (λ_0)	0.3 au
	Injection momentum spectral index	−5
	Injection scaling factor	1.2

Notes.
[a] This CME speed is reevaluated and reported in the DONKI database.
[b] These locations are given as the Carrington longitude and latitude.

Specifically, the Solar Terrestrial Relations Observatory (STEREO, described by M. L. Kaiser et al. 2008) CME Analysis Tool (StereoCAT,[12] G. Millward et al. 2013; M. Mays et al. 2015) can be utilized to calculate the CME speed with elimination of the projection effect by determining the CME's 3D trajectory through observations from multiple spacecraft. These 3D kinematic properties of CMEs are included in the Space Weather Database of Notifications, Knowledge, Information (DONKI[13]) database. We adopt 675 km s^{-1}, as reported by DONKI, as the accurate CME speed to calculate the flux rope parameters. Figure 1(b) shows the zoomed-in AR field with the chosen locations for the filament footpoints, as well as the polarity inversion line identified by EEGGL. Note that the input magnetogram is smoothed by a 5 × 5 pixel window in EEGGL to reduce the complexity of the photospheric magnetic field configuration. Based on empirical features of pre-event conditions (e.g., D. Borovikov et al. 2017; M. Jin et al. 2017b), EEGGL can offer an efficient parameter setup, including the location, orientation, and size of the flux rope and the magnetic field strength, as detailed in Table 1. With the force-imbalanced flux rope parameterized by EEGGL and inserted on top of the AR (see its 3D topology in Figure 1(c)), the CME propagation in the SC and IH is then modeled with time-accurate simulations.

2.3. Particle Solver

2.3.1. Governing Equation

As the SEP population likely forms out of the suprathermal tail of the solar wind, whose distribution is far from the Maxwellian (e.g., V. Pierrard & M. Lazar 2010; S. Kahler & A. Ling 2019; D. Lario et al. 2019), we characterize SEPs by a canonical distribution function $F(\boldsymbol{r},\ \boldsymbol{p},\ t)$ of coordinates ($\boldsymbol{r}$), momentum ($\boldsymbol{p}$), and time (t), such that the number of particles, dN, within the elementary volume, $d^3\boldsymbol{r}$, is given by the following normalization integral: $dN = d^3\boldsymbol{r}\int d^3\boldsymbol{p}\ F(\boldsymbol{r},\ \boldsymbol{p},\ t)$. In a magnetized moving plasma, it is convenient to consider the distribution function at any given point, $\boldsymbol{r}$, in a frame of reference moving with the local plasma bulk velocity, $\boldsymbol{u}(\boldsymbol{r},\ t)$. Also, we adopt the spherical coordinates ($p = |\boldsymbol{p}|$, $\mu = \boldsymbol{b}\cdot\boldsymbol{p}/p$, φ) in the momentum space with its polar axis aligned with the direction, $\boldsymbol{b} = \boldsymbol{B}/B$, of the magnetic field, $\boldsymbol{B}(\boldsymbol{r},\ t)$. Herewith, p indicates the magnitude of the particle momentum, B denotes the magnetic field amplitude ($|\boldsymbol{B}(\boldsymbol{r},\ t)|$), μ is the cosine value of the pitch angle, and φ is the phase angle of the particle Larmor gyration. The normalization integral in these new variables gives

$$dN = d^3\boldsymbol{r}\int_0^{+\infty} p^2 dp \int_{-1}^{1} d\mu \int_0^{2\pi} d\varphi\ F(\boldsymbol{r},\ p,\ \mu,\ \varphi,\ t). \tag{2}$$

Using the canonical distribution function, one can define a gyrotropic distribution function, $\mathcal{F}(\boldsymbol{r},\ p,\ \mu,\ t) = \frac{1}{2\pi}\int_0^{2\pi} d\varphi\ F(\boldsymbol{r},\ p,\ \mu,\ \varphi,\ t)$, to describe the particle motion averaged over the phase of gyration around the magnetic field. The omnidirectional distribution function, $f(\boldsymbol{r},\ p,\ t) = \frac{1}{2}\int_{-1}^{1} d\mu\ \mathcal{F}(\boldsymbol{r},\ p,\ \mu,\ t)$, is additionally averaged over the pitch angle. The normalization integral in Equation (2) becomes

$$\begin{aligned} dN &= 2\pi d^3\boldsymbol{r}\int_0^{+\infty} p^2 dp \int_{-1}^{1} d\mu\ \mathcal{F}(\boldsymbol{r},\ p,\ \mu,\ t) \\ &= 4\pi d^3\boldsymbol{r}\int_0^{+\infty} p^2 dp\, f(\boldsymbol{r},\ p,\ t). \end{aligned} \tag{3}$$

The acceleration and transport of energetic particles in IP space is described by the focused transport equation (e.g., T. G. Northrop 1963; E. Roelof 1969; J. Skilling 1971; P. A. Isenberg 1997; J. Kóta 1997, 2000; J. Kóta & J. Jokipii 2004; J. van den Berg et al. 2020), which accounts for the effects of particle displacement along the magnetic field, drift in the inhomogeneous magnetic field, adiabatic heating or cooling, and adiabatic focusing and particle scattering by the magnetic turbulence, forming the kinetic equation for the gyrotropic distribution function $\mathcal{F}(\boldsymbol{r},\ p,\ \mu,\ t)$:

$$\begin{aligned} &\frac{\partial \mathcal{F}}{\partial t} + \underbrace{\mu v\frac{\partial \mathcal{F}}{\partial s}}_{\text{Particle Streaming}} + \underbrace{(\boldsymbol{u}\cdot\nabla)\mathcal{F}}_{\text{Drift}} \\ &+ \underbrace{\frac{\partial \mathcal{F}}{\partial p}\frac{dp}{dt}}_{\text{Adiabatic Heating/Cooling}} + \underbrace{\frac{\partial \mathcal{F}}{\partial \mu}\frac{d\mu}{dt}}_{\text{Magnetic Focusing}} \\ &= \underbrace{\frac{\partial}{\partial \mu}\left(D_{\mu\mu}\frac{\partial \mathcal{F}}{\partial \mu}\right)}_{\text{Scattering}} + \underbrace{Q}_{\text{Additional Source/Sink}}, \end{aligned} \tag{4}$$

in which s is the distance along the magnetic field, $D_{\mu\mu}$ is the pitch-angle diffusion coefficient, and Q denotes the additional acceleration source or sink terms. In the diffusive limit of very high scattering rates, the distribution function is assumed to be isotropic, so that the focused transport equation reduces to the

---

[12] https://ccmc.gsfc.nasa.gov/tools/StereoCat/
[13] https://kauai.ccmc.gsfc.nasa.gov/DONKI/search/

Parker transport equation (E. N. Parker 1965):

$$\frac{\partial f}{\partial t} + \underbrace{(\boldsymbol{u}\cdot\nabla)f}_{\text{Drift}} - \underbrace{\frac{1}{3}(\nabla\cdot\boldsymbol{u})\frac{\partial f}{\partial \ln p}}_{\text{Adiabatic Heating/Cooling}} = \underbrace{\nabla\cdot(\overset{\leftrightarrow}{\kappa}\cdot\nabla\ f)}_{\text{Diffusion}} + \underbrace{Q}_{\text{Additional Source/Sink}}, \qquad (5)$$

where $\overset{\leftrightarrow}{\kappa} = D_{\|}\boldsymbol{bb}$ is the tensor of parallel diffusion along the magnetic field, and $D_{\|}$ is the parallel spatial diffusion coefficient. The term proportional to the divergence of $\boldsymbol{u}$ accounts for the adiabatic cooling for $\nabla\cdot\boldsymbol{u} > 0$, or the first-order Fermi acceleration in compression or shock wave fronts for $\nabla\cdot\boldsymbol{u} < 0$ (E. Fermi 1949). Although less accurate than the focused transport equation (see Equation (4)), the Parker transport equation (see Equation (5)) remains widely used in SEP studies, since it well describes the acceleration at the shock wave front, where the scattering is enhanced by the self-excited turbulence, and it captures the effects of interplanetary magnetic field (IMF) and IP plasma properties on the SEP transport process. However, far upstream of the shock wave, where the scattering rate is much lower and particle propagation is nearly scatter-free, the focused transport equation would outperform the Parker one (e.g., D. V. Reames 2021, and references therein). Nevertheless, we adopt Equation (5) for the SEP numerical modeling in this study.

2.3.2. M-FLAMPA

In the SWMF, the Multiple Field-Line-Advection Model for Particle Acceleration (M-FLAMPA, I. V. Sokolov et al. 2004; D. Borovikov et al. 2018, 2019) has been developed to simulate the particle acceleration and transport processes, where the particles are accelerated at the shocks driven by CMEs through the first-order Fermi acceleration mechanism (E. Fermi 1949). With no loss in generality, M-FLAMPA reduces a 3D problem of particle propagation in the IMF to a multitude of simpler 1D problems of particle transport along a single line of the IMF. As the simulation begins, AWSoM-R and M-FLAMPA run simultaneously. At each time step, the time-evolving magnetic field lines, as well as the plasma properties, are extracted from the AWSoM-R solutions, and the particle distribution function is solved along them (D. Borovikov et al. 2015, 2018). Moreover, as proposed by I. V. Sokolov et al. (2004), novel mathematical approaches are applied to the extracted magnetic field lines to sharpen the shock wave front, thus enhancing the efficiency of the DSA process.

In M-FLAMPA, the particles are assumed to couple with the magnetic field lines. The particle motions consist of the displacement of the particle's guiding center along the IMF line, and the joint advection of both the guiding center and the IMF line together with the plasma where the magnetic field is frozen. Mathematically, this method employs the Lagrangian coordinate, $\boldsymbol{x}_{\text{L}}$, which stays with the advecting fluid elements in space (L. D. Landau & E. M. Lifshitz 1987). Herewith, the partial time derivative at the constant Lagrangian coordinate, $\boldsymbol{x}_L$, and the time, τ, is denoted as d/dt or $\partial/\partial\tau$, while the notation $\partial/\partial t$ denotes the partial time derivative at the constant Eulerian coordinate, $\boldsymbol{x}$, with the relations $\partial/\partial\tau = d/dt = \partial/\partial t + \boldsymbol{u}\cdot\nabla$. Certain terms in Equation (5) can be expressed in terms of Lagrangian derivatives and the spatial derivative along magnetic field lines, combining with the plasma motion equations. Equation (5) can be eventually rewritten as (D. Borovikov et al. 2018, 2019; I. V. Sokolov et al. 2023)

$$\frac{\partial f}{\partial \tau} = \frac{df}{dt} = -\frac{1}{3}\frac{D\ln\rho}{Dt}\frac{\partial f}{\partial \ln p} + \nabla\ \cdot(\overset{\leftrightarrow}{\kappa}\cdot\nabla f) + Q, \qquad (6)$$

where ρ denotes the mass density of the plasma.

In addition, the Strang splitting method (e.g., G. Strang 1968; S. MacNamara & G. Strang 2016) is applied in M-FLAMPA to split the advection and diffusion terms, in order to solve Equation (6) efficiently. Here, we implement the high-resolution Poisson bracket scheme for advections (I. V. Sokolov et al. 2023) and use the theoretical derivations for the diffusion coefficient based on the quasi-linear theory (J. R. Jokipii 1966) and the turbulent magnetic field (see G. Li et al. 2003; I. V. Sokolov et al. 2004; D. Borovikov et al. 2019, and references therein). More details are described in Sections 2.3.3 and 2.3.4.

2.3.3. Implementation of the I. V. Sokolov et al. (2023) Poisson Bracket Scheme

In order to simulate the fluxes of shock-accelerated SEPs, we solve the kinetic equation throughout the whole computational domain, including the shock wave region, with the DSA mechanism in the heart of our SEP model. In this case, it is important to use a particle-number-conserving scheme. Otherwise, the prediction for SEP fluxes may be contaminated by fake particle productions or disappearances due to approximation errors at high spatial gradients near the shock wave front.

In classical mechanics (L. Landau & E. Lifshitz 1960), the Poisson bracket for the distribution function, $F(\boldsymbol{r}, \boldsymbol{p}, t)$, is introduced as

$$\{F; H\} \equiv \sum_{\ell}\{F; H\}_{q_\ell, p_\ell} = \sum_{\ell}\left(\frac{\partial F}{\partial q_\ell}\frac{\partial H}{\partial p_\ell} - \frac{\partial H}{\partial q_\ell}\frac{\partial F}{\partial p_\ell}\right). \qquad (7)$$

Here, H represents the Hamiltonian function, p_ℓ and q_ℓ are the canonical coordinates for momentum and position, respectively, and ℓ denotes the ℓth degree of freedom. Along the Hamiltonian trajectory, where $dq_\ell/dt = \partial H/\partial p_\ell,\ dp_\ell/dt = -\partial H/\partial q_\ell,\ \forall\,\ell$, the time evolution of the distribution function is governed by the Poisson bracket with the Hamiltonian function:

$$\frac{dF}{dt} = \frac{\partial F}{\partial t} + \{F; H\} = 0, \qquad (8)$$

This fundamental conservation law, known as the *Liouville theorem* (J. Liouville 1838), states that the distribution function remains constant along the Hamiltonian trajectory.

Based on the integral relations for Poisson brackets, I. V. Sokolov et al. (2023) have developed a computationally efficient scheme for solving kinetic equations using the finite volume method. This newly developed Poisson bracket scheme conserves the number of particles and possesses the total-variation-diminishing (TVD, e.g., I. V. Sokolov et al. 2006a; L. Krivodonova & A. Smirnov 2021; G. Tóth 2023) property with second order of accuracy in space, thus ensuring high-resolution numerical results. With the Poisson bracket scheme, Equation (5) can be reformulated as

$$\frac{B}{\delta s}\left\{f_{j,k}\,;\,\frac{\delta s}{B}\frac{p^3}{3}\right\}_{\tau,\,p^3/3}=\frac{B}{\delta s}\frac{\partial}{\partial s_L}\left(\frac{D_{\|}}{B\delta s}\frac{\partial f_{j,k}}{\partial s_L}\right), \tag{9}$$

where $f_{j,k}(s_L, p^3/3, \tau)$ is the omnidirectional distribution function along the field line that has been initially traced through the grid point, $\boldsymbol{x}_{j,k}$, back to the inner boundary of the SC domain and outer boundary of the IH domain. These grid points are uniformly spaced in longitude and latitude with the indices j and k, respectively, on the spherical surface at $r = 2.5\,R_s$. Herewith, $\delta s = ds/ds_L$, where ds is the element of the length introduced above (see Equation (4)), s, along the magnetic field line, and ds_L is the mesh size in the Lagrangian coordinate, s_L. More details on the derivations of Equation (9) can be found in Section 4 of I. V. Sokolov et al. (2023).

By the Strang splitting method (G. Strang 1968; S. MacNamara & G. Strang 2016), at each time step, we first solve the advection equation in the phase space:

$$\left\{f_{j,k}\,;\,\frac{\delta s}{B}\frac{p^3}{3}\right\}_{\tau,\,p^3/3}=0, \tag{10}$$

where the Hamiltonian function is $H \equiv (\delta s/B)p^3/3$, with τ and $p^3/3$ being the two canonical coordinates as we solve the time-accurate transport equation for SEPs.

Note that the Poisson bracket scheme is applicable to various types of kinetic equations that can be formulated in terms of Poisson brackets. It has been demonstrated by I. V. Sokolov et al. (2019) that the focused transport equation (see Equation (4)) can be formulated into multiple Poisson brackets, showing the potential to study the pitch-angle dependence in testing cases using the Poisson bracket scheme. In this work, we solve the Parker transport equation (see Equation (5)) for the omnidirectional distribution function, notated as $f(\boldsymbol{r}, p, t)$, as a first implementation of the Poisson bracket scheme in M-FLAMPA. More sophisticated numerical models that take into account the pitch-angle dependence for the distribution function will be investigated in the future.

2.3.4. Particle Diffusion

The interaction between the energetic protons and turbulent magnetic fields is modeled by diffusion along time-evolving magnetic field lines. Following Equation (10), within each time step, the transport equation is subsequently solved for spatial diffusion along each field line in M-FLAMPA:

$$\frac{\partial f_{j,k}}{\partial \tau}=\frac{B}{\delta s}\frac{\partial}{\partial s_L}\left(\frac{D_{\|}}{B\delta s}\frac{\partial f_{j,k}}{\partial s_L}\right), \tag{11}$$

where the spatial diffusion coefficient along the magnetic field, $D_{\|}$, can be derived in the usual manner from the scattering integral with respect to the particle pitch angle, $D_{\mu\mu}$ (e.g., J. R. Jokipii 1966; J. A. Earl 1974; M. A. Lee 1982, 1983; J. Kóta 2000):

$$D_{\|}=\frac{v^2}{8}\int_{-1}^{1}\frac{(1-\mu^2)^2}{D_{\mu\mu}}\,d\mu, \tag{12}$$

$$D_{\mu\mu}=\frac{\pi\omega_{ci}k}{2B^2/\mu_0}(1-\mu^2)\sum_{+,\,-}I_{\pm}(k), \tag{13}$$

in which $v = |\boldsymbol{v}|$ denotes the proton speed, μ_0 is the vacuum permeability, and $\omega_{ci} = eB/m$ is the cyclotron frequency of protons, with e being the proton charge. $I_{\pm}(k)$ denotes the spectral energy density of turbulent waves, which propagate parallel (I_+) and antiparallel (I_-) to the magnetic field. The wavenumber taken at $k = \omega_{ci}/(v\,|\mu|)$ satisfies the resonance condition (M. A. Lee 1982; D. Borovikov et al. 2019). Both turbulent wave spectra are assumed to follow Kolmogorov's power law with an index of $-5/3$ (A. Kolmogorov 1941; V. E. Zakharov et al. 2012). At the current stage, our model does not account for the contributions of the self-generated wave turbulence by energetic particles. More details on the assumptions, considerations, and derivations of the model are given by I. V. Sokolov et al. (2009) and D. Borovikov et al. (2019). Finally, the parallel diffusion coefficient, $D_{\|}$, can be expressed in terms of the mean free path (MFP), $\lambda_{\|}$, and the proton speed (e.g., I. V. Sokolov et al. 2004):

$$D_{\|}=\frac{1}{3}\lambda_{\|}v, \tag{14}$$

with different treatments of $\lambda_{\|}$ in the upstream and downstream regions of the shock in M-FLAMPA. In the upstream region of the shock, the MFP can be approximated as (G. Li et al. 2003; G. Li & G. Zank 2005; G. Zank et al. 2007):

$$\lambda_{\|}=\lambda_0\left(\frac{r}{1\ \text{au}}\right)\left(\frac{pc}{1\ \text{GeV}}\right)^{1/3}, \tag{15}$$

in which λ_0 is the MFP for 1 GeV particles at 1 au and it is a free parameter in the model. With the relativistic relations between the proton speed, momentum, and kinetic energy, the parallel diffusion coefficient, $D_{\|}$ in Equation (14), can be expressed as

$$D_{\|}=\frac{1}{3}c\,\lambda_0\left(\frac{r}{1\ \text{au}}\right)\left[\frac{E_k(E_k+2E_{\text{p0}})}{(1\ \text{GeV})^2}\right]^{1/6}\times\left[\frac{E_k(E_k+2E_{\text{p0}})}{(E_k+E_{\text{p0}})^2}\right]^{1/2}, \tag{16}$$

where c denotes the speed of light, E_k denotes the kinetic energy of energetic protons, and $E_{\text{p0}} = m_{\text{p}}c^2 = 938.1$ MeV is the proton rest energy, with m_{p} being the proton rest mass. It can be seen from Equation (16) that the upstream parallel diffusion coefficient approximately follows $D_{\|} \propto r \cdot E_k^{2/3}$ for the protons in the energy range from keV to MeV.

Note that different parameter configurations of the MFP and the parallel diffusion coefficient may lead to different results (e.g., K. Kecskeméty et al. 2009; L. Zhao et al. 2016, 2024). In order to justify the validity of the choice adopted for $D_{\|}$, we refer to a recent study by X. Chen et al. (2024), which examines the power spectrum density of the magnetic turbulence measured by the Solar Wind Electrons, Alphas, and Protons (SWEAP, J. C. Kasper et al. 2016) and FIELDS (S. D. Bale et al. 2016) instruments on board the Parker Solar Probe (PSP, N. Fox et al. 2016). Based on the PSP observations in its Orbits 5–13, X. Chen et al. (2024) derived an empirical formula of the parallel diffusion coefficient for 100 keV to

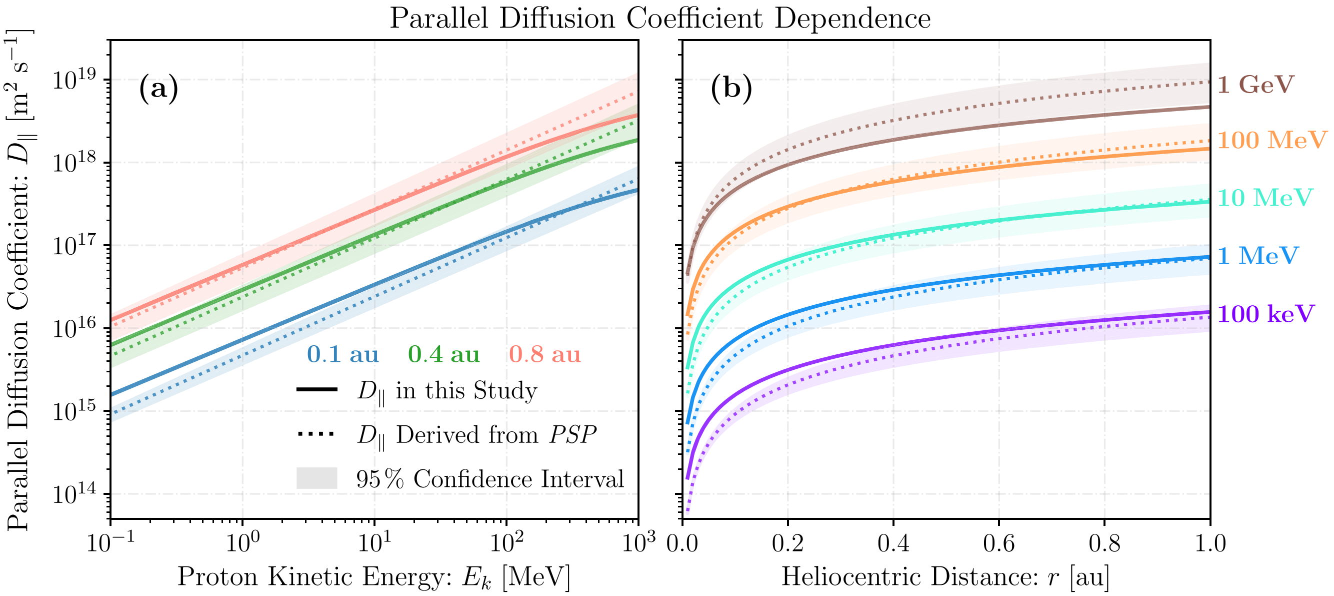

Figure 2. Parallel diffusion coefficient in the upstream shock region used in this study (solid lines) in comparison with that derived by X. Chen et al. (2024) from the PSP observations (dotted lines, with the 95% confidence interval plotted as shaded areas). (a) Dependence of parallel diffusion coefficient on the proton kinetic energy at heliocentric distances of 0.1, 0.4, and 0.8 au, plotted in blue, green, and red, respectively. (b) Dependence of parallel diffusion coefficient on the radial distance for proton kinetic energies of 100 keV, 1 MeV, 10 MeV, 100 MeV, and 1 GeV, plotted in purple, blue, cyan, orange, and brown, respectively.

1 GeV energetic protons in the inner heliosphere:

$$D_\parallel = (5.16 \pm 1.22) \times 10^{14} \left(\frac{r}{1\ \mathrm{au}}\right)^{1.17\pm0.08} \times \left(\frac{E_k}{1\ \mathrm{keV}}\right)^{0.71\pm0.02} [\mathrm{m^2\ s^{-1}}]. \tag{17}$$

With a similar index simplified from Equation (16) for the keV to MeV protons, i.e., $D_\parallel \propto r \cdot E_k^{2/3}$, we compare the dependence of the diffusion coefficient adopted in M-FLAMPA on the heliocentric distance (see Figure 2(a)) and the proton energy (see Figure 2(b)) with those derived by X. Chen et al. (2024) from the interplanetary turbulence level as observed by PSP. In this work, we take λ_0 in Equation (15) to be 0.3 au, which is consistent with the results of X. Chen et al. (2024). As shown in Figure 2, the comparison demonstrates a perfect agreement within the 95% confidence interval.

In the downstream region of the shock, the diffusion coefficient is calculated self-consistently through the total Aflvén wave intensity obtained from the MHD simulation. Following Equations (12) and (13), we introduce a minimum wavenumber, k_0, below which the turbulence level becomes negligible. In this way, the downstream MFP is derived by only considering $I_\pm(k)$ for $k \geqslant k_0$ in Equation (13), corresponding to sufficiently small spatial scales. With the derivations shown by D. Borovikov et al. (2019), we have

$$\lambda_\parallel = \frac{81}{7\pi}\left(\frac{B}{\delta B}\right)^2 \frac{r_{\mathrm{L0}}^{1/3}}{k_0^{2/3}} \times \left(\frac{pc}{1\ \mathrm{GeV}}\right)^{1/3}, \tag{18}$$

in which δB is the turbulent field strength, and $r_{\mathrm{L0}} = 1\ \mathrm{GeV}/ceB$ is the Larmor radius for the particle momentum being 1 GeV$/c$. Herewith, we consider

$$k_0 = \frac{2\pi}{L_{\max}(r)}, \tag{19}$$

with the maximum spatial scale in the turbulence, $L_{\max}(r) = 0.03\, r$ (e.g., W. H. Matthaeus et al. 1999; F. Pucci et al. 2016; D. Borovikov et al. 2019, and references therein), which gives a relatively comparable magnitude of the MFP downstream and upstream of the shock as shown in the Figure in Section 4.4.5.. Besides, in order to compensate for the eroded width of the shock wave front due to the finite mesh size in the MHD simulations ($\sim 0.1\, R_s$), the parallel diffusion coefficient for the low-energy particles is artificially enhanced to

$$D_\parallel = \max\{D_\parallel,\ D_{\min}\}, \tag{20}$$

where $D_{\min} = 0.1\, R_s \times 10^5\ \mathrm{m\ s^{-1}}$, as used by I. V. Sokolov et al. (2004) and D. Borovikov et al. (2018).

Using Equations (12)–(20), the diffusion equation in Equation (11) can be solved along each individual magnetic field line. It is important to note that this approach does not account for perpendicular diffusion due to the field line random walk and particle decoupling from field lines, which still remains a subject of active research and discussions within the community (e.g., T. Laitinen et al. 2013, 2016, 2018; A. Shalchi 2019, 2021; R. Chhiber et al. 2021) and will be implemented in our model in the future.

2.3.5. Particle Injection

Given the established dynamics that governs particle acceleration and transport, the next essential component of our model is the injection of particles into the shock acceleration process. In our simulations, the boundary condition at low energies for the omnidirectional distribution function is based on the assumption of a suprathermal tail extending from the plasma thermal energy to the injection energy or the equivalent momentum (see also I. V. Sokolov et al. 2004). This tail is assumed to follow a power law, $f \propto p^{-5}$, commonly observed in the solar wind (e.g., G. Gloeckler 2003; L. Fisk & G. Gloeckler 2006, 2008, and references therein):

$$f(p_{\text{inj}}) = \frac{c_i}{2\pi} \frac{n_{\text{p}}}{(2m_{\text{p}}k_{\text{B}}T_{\text{p}})^{3/2}} \left(\frac{\sqrt{2m_{\text{p}}k_{\text{B}}T_{\text{p}}}}{p_{\text{inj}}} \right)^5, \tag{21}$$

where k_{B} is the Boltzmann constant, and n_{p} and $k_{\text{B}}T_{\text{p}}$ denote the ambient plasma density and temperature in energy units calculated from the AWSoM-R simulation, respectively. Here, p_{inj} is the injection momentum corresponding to the injection energy, which is set to be 10 keV at any location of the shock wave front (e.g., D. C. Ellison et al. 1990; J. Giacalone & J. Kóta 2007). Also, the amplitude of the injected particles is determined by the so-called injection coefficient, c_i, which indicates the fraction of suprathermal protons and can be derived from

$$4\pi \int_{\sqrt{2m_{\text{p}}k_{\text{B}}T_{\text{p}}}}^{+\infty} p^2 f(p)\, dp = c_i n_{\text{p}}. \tag{22}$$

The injection coefficient, c_i, is assumed to be 1 in the simulations. In order to match the observation, a scaling factor, 1.2, is used to scale up the calculated particle flux (L. Zhao et al. 2024). A scaling factor greater than 1 indicates that there are actually more seed particles injected into the shock acceleration than what is calculated by Equation (21). Since the wave turbulence self-generated by the streaming protons (e.g., C. Ng & D. Reames 1994; R. Vainio 2003; R. Treumann 2009) is not included in the simulation, the acceleration and transport of energetic protons remain unaffected by such a scaling factor (L. Zhao et al. 2024).

To summarize, Table 1 recapitulates the key input parameters used for this study, as described through Section 2.

3. The 2013 April 11 SEP Event: Overview

The SEP event on 2013 April 11 was one of the widespread SEP events observed in solar cycle 24 (e.g., N. Dresing et al. 2014; N. Gopalswamy et al. 2015; I. Richardson et al. 2014; M. Paassilta et al. 2018). D. Lario et al. (2014) studied this event using observations from multiple spacecraft, including the STEREO Ahead/Behind (STA/STB, described by M. L. Kaiser et al. 2008), the Solar and Heliospheric Observatory (SOHO, described by V. Domingo et al. 1995), the Advanced Composition Explorer (ACE, described by E. C. Stone et al. 1998), the Geostationary Operational Environmental Satellite (GOES, described by W. P. Menzel & J. F. Purdom 1994), and the Wind spacecraft (described by, e.g., R. Harten & K. Clark 1995). They also analyzed the corresponding solar sources of this event by examining extreme ultraviolet (EUV) wave observations and white-light (WL) coronagraph images from STA, STB, and the Atmospheric Imaging Assembly (AIA, J. R. Lemen et al. 2012) on board the Solar Dynamics Observatory (SDO, W. D. Pesnell et al. 2012). Furthermore, this particular event shows high Fe/O abundance ratios observed by particle detectors on board STB and ACE (see Figure 4 of D. Lario et al. 2014 and more details given by C. Cohen et al. 2014).

In this event, the filament eruption that triggered the CME responsible for this SEP event has been investigated by multiple studies (e.g., P. Vemareddy & W. Mishra 2015; B. Joshi et al. 2016; R.-Y. Kwon & A. Vourlidas 2017; E. Palmerio et al. 2018; A. Fulara et al. 2019; E. K. Kilpua et al. 2019; H. Pan et al. 2022). On 2013 April 11, an M6.5 X-ray flare erupted from the NOAA AR 11719, located at Stonyhurst heliographic latitude +9° and longitude −12° (N09E12) as viewed from Earth. The soft X-ray emission began at 06:55 UT and peaked at 07:16 UT. Both STB and Wind observed type III radio bursts associated with this eruption from the highest frequencies that the instruments can detect (∼16 MHz) starting at about 06:58 UT, while STA observed the type III burst only at frequencies below 1 MHz starting around 07:00 UT.

An associated CME was then observed by the C2 coronagraph of the Large Angle and Spectrometric Coronagraph (LASCO, G. E. Brueckner et al. 1995) on board SOHO at 07:24 UT, and by the COR1 coronagraph (W. T. Thompson et al. 2003) of the Sun Earth Connection Coronal and Heliospheric Investigation (SECCHI, R. A. Howard et al. 2008) telescopes on board both STA and STB at 07:54 UT (C. Cohen et al. 2014). The LASCO observations (e.g., Section 3.4 of B. Joshi et al. 2016) indicate that this is a moderately fast halo CME, with the plane-of-sky CME speed of 861 km s^{-1} as reported in the Coordinated Data Analysis Web (CDAW) CME catalog[14] (S. Yashiro et al. 2004; N. Gopalswamy et al. 2009). The plane-of-sky CME speed is also reported as 668 km s^{-1} and 590 km s^{-1} by STA/SECCHI and STB/SECCHI, respectively, in the corresponding catalogs[15] (E. Robbrecht et al. 2009). By combining these multipoint spacecraft observations, the CME speed is estimated to be over 1000 km s^{-1}, as reported by J. Park et al. (2017). However, M. Mays et al. (2015) and M. Dumbović et al. (2018) found that such a value can lead to too early an arrival of the CME at Earth in numerical modeling. The reevaluated CME speed is 675 km s^{-1}, as listed in the DONKI database. A type II radio burst was observed by both STB and Wind starting at 07:10 UT and ending around 15:00 UT in the range of frequencies from 10 MHz to 200 kHz, as reported by D. Lario et al. (2014) and J. Park et al. (2015).

Figure 3(a) shows the longitudinal locations of Earth, STA, and STB, as well as the corresponding nominal IMF lines shortly before the CME eruption on 2013 April 11, as viewed from the north pole of the Sun. The exact observation locations in the heliographic rotating (HGR) coordinate system are provided in Table 2. Here, the nominal IMF lines assume a Parker spiral field with a constant solar wind speed (E. N. Parker 1958) and an analytical solution taken from the Solar-Mach tool[16] (J. Gieseler et al. 2023). Here, we estimate the solar wind speed (U_{sw}) by averaging the in situ plasma measurements from the NASA Goddard Space Flight Center (GSFC) OMNI data set[17] (J. King & N. Papitashvili 2005) over a 12 hr window prior to the eruption. The resulting solar wind speed is approximately 363 km s^{-1} at Earth, $\gtrsim$500 km s^{-1} at STA, and 327 km s^{-1} at STB, giving the nominal magnetic footpoint separations of 110°–130° between pairs of observation locations, as listed in Table 2.

In Figure 3(a), the orientation of the CME flux rope derived from EEGGL and inserted at 07:24 UT is marked by a blue arrow. The flux rope is placed above AR 11719, centered at $(69^{\circ}\!.5,\ 14^{\circ}\!.5)$ in Carrington longitude and latitude, as shown in

---

[14] https://cdaw.gsfc.nasa.gov/CME_list/

[15] https://secchi.nrl.navy.mil/cactus/

[16] https://solar-mach.github.io/

[17] https://omniweb.gsfc.nasa.gov/

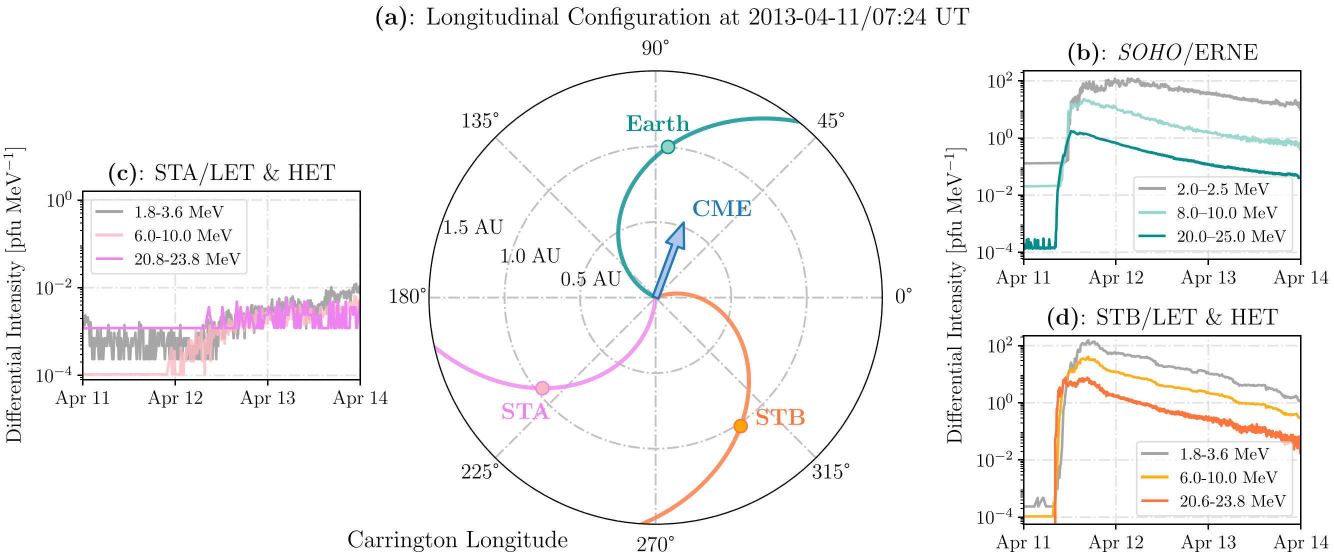

Figure 3. Overview of the 2013 April 11 SEP event. (a) Longitudinal configuration of Earth, STA, and STB locations (circles) with the nominal IMF lines connecting them to the Sun, as taken from the Solar-Mach tool (J. Gieseler et al. 2023) and viewed from the north pole of the Sun, plotted in the HGR coordinates in green, pink, and orange, respectively. The blue arrow shows the CME orientation for this event. (b), (c), (d) Measurements of energetic particles by SOHO/ERNE near Earth, STA/LET and HET, and STB/LET and HET respectively.

Table 2
Solar Wind and IMF Parameters at Different Locations

Location	ϕ_C (deg)	θ_C (deg)	r (au)	U_{sw} (km s^{-1})	ϕ_F (deg)	$\Delta\phi_{F,AR}$ (deg)
Earth	85.3	−5.9	1.00	363	154.0	84.5
STA	218.7	7.2	0.96	514	264.7	−164.8
STB	303.5	2.3	1.02	327	21.8	−47.7

Note. The list of observation locations included in this study, along with key parameters: the Carrington longitude (ϕ_C), the Carrington latitude (θ_C), and the heliocentric distance (r); the in situ solar wind bulk speed (U_{sw}); the Carrington longitude of the magnetic footpoint following the nominal IMF (ϕ_F); and the angular distance between the magnetic footpoint derived from the nominal IMF and the source region from which the CME originates ($\Delta\phi_{F,AR}$). Here, negative and positive values represent the eastward and westward directions toward the footpoints, respectively.

Figure 1(b). In Table 2, we show the angular distance between the nominal magnetic footpoint and the parent AR from which the CME originates ($\Delta\phi_{F,AR}$). These values demonstrate that the magnetic footpoint of STB is the closest to AR 11719 among the three observers, followed by Earth, and that STA is the farthest. Note that the coronal magnetic field can be highly complex and that this estimation can be limited. Alternative methods for calculating these angular distances are presented in Section 2 of D. Lario et al. (2014).

Figures 3(b)–(d) show the energetic particle time–intensity profiles measured by (b) the Energetic and Relativistic Nuclei and Electron instrument (ERNE, J. Torsti et al. 1995; E. Valtonen et al. 1997) on SOHO; (c) the Low Energy Telescope (LET, R. A. Mewaldt et al. 2008) and High Energy Telescope (HET, T. Von Rosenvinge et al. 2008) on STA; and (d) LET and HET on STB. We choose three energy channels for each spacecraft as shown in Figures 3(b)–(d), as representative of particle measurements[18] at low, intermediate, and high energies, respectively. It can be found that

1. In Figures 3(b)–(d), the onset phase of the SEP event appears sharper at STB than at Earth, especially in the higher-energy channels (20.6–23.8 MeV in STB/HET, and 20.0–25.0 MeV in SOHO/ERNE). A more detailed comparison of the onset phase of Earth and STB can be found in Figure 5 of D. Lario et al. (2014). Moreover, the low-energy channels (1.8–3.6 MeV in STB/LET, and 2.0–2.5 MeV in SOHO/ERNE) in Figures 3(b)–(d) show that the SEP fluxes at STB decay more quickly than those at Earth.
2. While noticeable SEP fluxes are observed at both Earth and STB, there is only a slight enhancement of particle measurements at STA, as shown in Figure 3(c). This disparity at STA is consistent with the large longitudinal distance between the source AR and the nominal magnetic footpoint of STA (also see Table 2).

In the following, we will show the results of numerical simulations of this event using the models described in Section 2 and compare them with the measurements of observed particles.

4. Results and Discussion

In this section, we present the results for each component of the model. In Section 4.1, we show the results of steady-state solar wind simulations for a period of 27 days centered at 2013 April 11/06:04 UT. With this steady-state solar wind solution, the flux rope is inserted within AR 11719 from which the CME erupts. We show the initial state and evolution of the CME, and compare the synthetic WL images with observations in Section 4.2. In Section 4.3, we describe our newly developed shock-capturing tool and illustrate how the shock surface is identified and its evolution in the low solar corona. In Section 4.4, we highlight our M-FLAMPA SEP simulation results and compare them with in situ particle measurements.

4.1. Steady-state Solar Wind

Taking the processed GONG magnetogram shown in Figure 1(a) and the parameters listed in Table 1 as inputs, the

---

[18] Hereafter, “pfu” refers to the particle flux unit, defined as 1 pfu = 1 count cm^{-2} s^{-1} sr^{-1}.

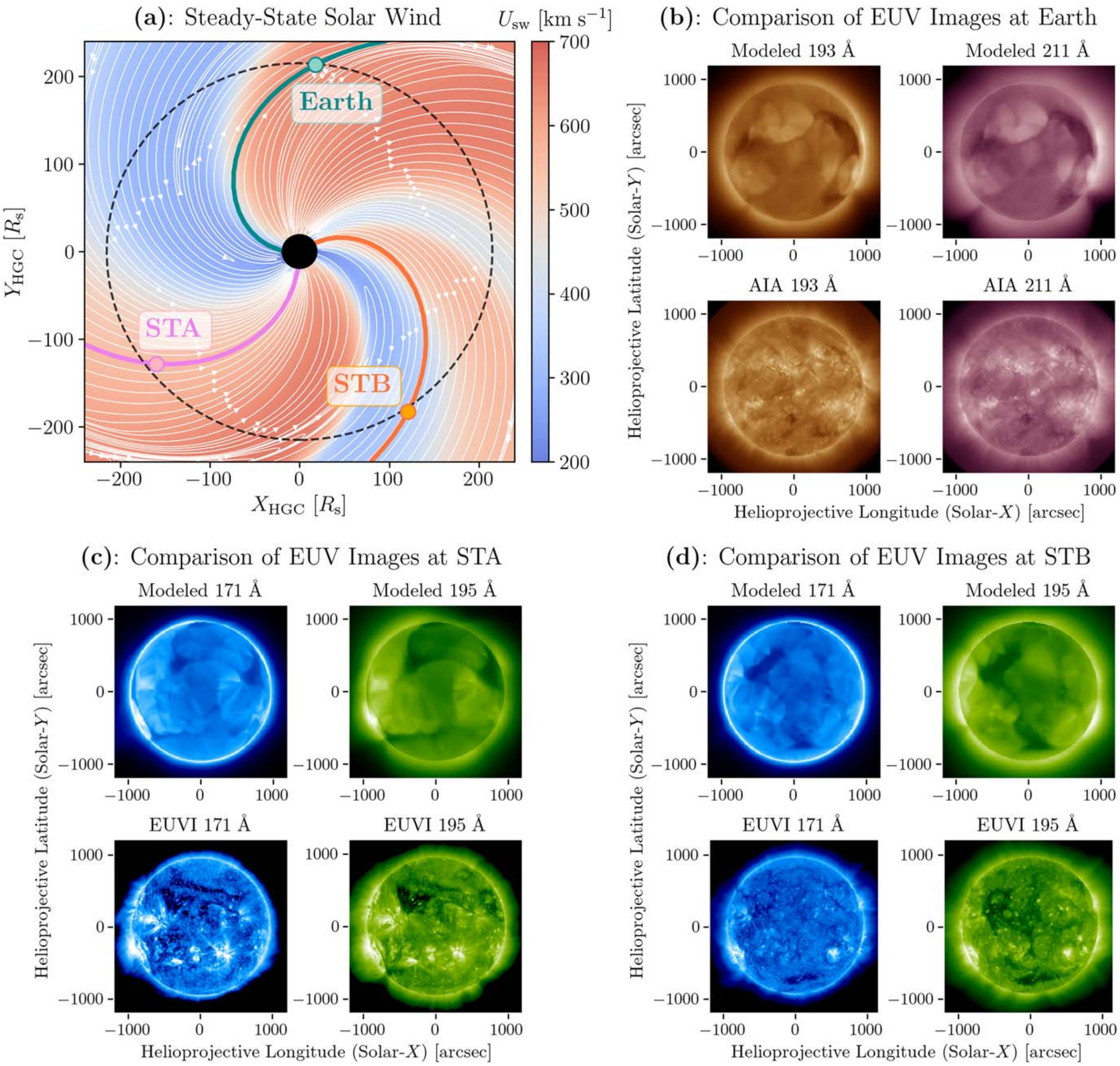

Figure 4. Steady-state simulation results by AWSoM-R solving the stream-aligned MHD equations. (a) Background solar wind speed in the solar equatorial plane, with the Carrington heliographic (HGC) coordinates used. The white curves with arrows indicate the magnetic field lines, and those connecting to Earth, STA, and STB are plotted in green, pink, and orange, respectively. The black dashed circle represents a heliocentric distance of 1 au. The black solid circle at the center is the lower boundary of the IH in our simulations (20 $R_{\rm s}$). (b), (c), (d) Comparison of the EUV images at Earth, STA, and STB, respectively. The modeled images at 193 Å and 211 Å wavelengths are compared with those observed by SDO/AIA near Earth, and images at 171 Å and 195 Å wavelengths are compared with those observed by EUVI on board STA and STB, respectively. Helioprojective longitude and latitude are shown in the modeled and observed images for spatial references.

stream-aligned AWSoM-R model calculates the properties of the 3D solar wind plasma. The solar wind speed in the solar equatorial plane in the IH is shown in Figure 4(a), plotted with the locations of Earth, STA, and STB, as well as the magnetic field lines connecting them to the inner boundary of the IH. As seen in Figure 4(a), Earth and STA are located in regions with relatively fast solar wind ($>$500 km s^{-1}), while the solar wind is relatively slow at STB ($\simeq$300 km s^{-1}), comparable to the values in Table 2. We also plot other magnetic field lines in the equatorial plane as white curves with arrows, demonstrating the alignment of the magnetic field and the solar wind plasma stream (see Section 2.1 and I. V. Sokolov et al. 2022).

We use the simulated steady-state solar wind electron density and temperature to synthesize the LOS EUV images, which are compared with the multiwavelength EUV observations[19] from SDO/AIA and the Extreme UltraViolet Imager (EUVI, J.-P. Wuelser et al. 2004) on board STA and STB. The comparisons between simulations and observations are shown in Figures 4(b)–(d), corresponding to 193 Å and 211 Å bands for SDO/AIA, and 171 Å and 195 Å for STA/EUVI and STB/EUVI. For each comparison, the top row shows the model-synthesized LOS EUV images, and the bottom row shows the

---

[19] https://sdac.virtualsolar.org/cgi/search

observation results. The key findings from the EUV image comparisons in Figures 4(b)–(d) are the following.

1. The simulation results exhibit reasonable consistency with the observations in matching the relative brightness on a global scale, capturing the positions of major coronal holes (CHs) and ARs. This agreement indicates that the stream-aligned AWSoM-R model is able to reproduce the overall 3D structure of the density and temperature in the low solar corona.
2. The CHs in the northern hemisphere are captured in simulations from the STA and STB views, and the narrow CH close to the south pole is also reproduced in simulations from the STB view, as shown in Figures 4(c) and (d). Although the simulated CHs in the northern hemisphere are visible from Earth's point of view, they are darker than SDO/AIA observations in Figure 4(b). As discussed by N. Sachdeva et al. (2023), solar CHs contain small-scale, closed field-line loops and magnetic flux that add to their brightness. In contrast, the numerical simulation often lacks these small-scale features, leading to darker CHs in the synthetic images.
3. As shown in Figures 4(b)–(d), the stream-aligned AWSoM-R model reproduces the bright ARs on the west limb from the Earth view, and the ARs on both the west and east limbs from the STA and STB views. However, the small-scale ARs in the center of the EUV images observed are either partially visible or not present in the model results. This discrepancy can be attributed to a combination of factors, including the uncertainties of observational data prepared for the synoptic map, the evolution of all ARs, particularly near the solar maximum, as well as the order of accuracy in the modeling scheme (e.g., L. Bertello et al. 2014; T. I. Gombosi et al. 2021; N. Sachdeva et al. 2021, 2023, and references therein).

Despite the discrepancies in some fine structures, such as CHs and ARs, the model demonstrates generally good agreement in terms of the overall brightness, as well as the spatial location and scale of these features, indicating high simulation performance in capturing the global structure in the low corona (C. Downs et al. 2010; N. Sachdeva et al. 2019, 2021). We also note that the radius of the source surface of the PFSS model is set to be 2.5 R_s in this work, as described in Section 2.1. Adjusting the outer boundary of the PFSS model may lead to an improved background solar wind solution (e.g., C. Lee et al. 2011; Z. Huang et al. 2024a, and references therein), which is important in modeling the propagation of CMEs and SEPs. Overall, the comparisons shown in Figures 4(b)–(d) validate the synthesized EUV observables and suggest the readiness of steady-state solar wind solutions for subsequent simulations.

4.2. CME Eruption and Propagation

After obtaining steady-state solar wind solutions, a force-imbalanced GL magnetic flux rope (S. E. Gibson & B. Low 1998) and its entrained plasma are placed on top of the parent AR (AR 11719 for this event). After the insertion, we do not change the velocity of the initial states to drive self-similar evolution. Figure 5 presents the time evolution of the CME in 3D, at $t = 0$, 6, 12, and 24 minutes from the top panels to the bottom. In each panel, the magnetic field lines are plotted as solid lines, and the colors from blue to red represent the radial magnetic field strength on the 1.1 R_s sphere and along the field lines. A plane cut depicts the distribution of the plasma speed in the left column of Figure 5 and the $\Delta U = \Delta x \, \nabla \cdot \boldsymbol{u}$ value for the divergence of the velocity field times the cell size in the right column of Figure 5. The color bars for different parameters are shown at the bottom of each panel. In Figures 5(c), (e), and (g), we can see that the evolution of the flux rope starts with a rapid acceleration to a speed greater than 1200 km s^{-1} in the low corona. The fast propagation of the flux rope drives a fast-mode MHD shock ahead of it, corresponding to the interface between the magenta and blue regions. As the flux rope propagates outward, it interacts with the background magnetic field, changing the field topology. The interaction is evident in the bent field lines downstream of the shock, as shown in Figures 5(e)–(h).

Here, we compare the model-synthesized WL images with observations (see footnote 19) to validate the propagation direction of the CME flux rope. In our model, the synthetic WL images are created by integrating the Thomson-scattered light along the LOS that comprises the image (e.g., A. Hayes et al. 2001; H. Morgan et al. 2006). As illustrated in Figure 6, we compare the model-synthesized WL images with those captured by LASCO/C2 (Figures 6(a) and (b)), STA/COR1 (Figures 6(c) and (d)), and STB/COR1 (Figures 6(e) and (f)) coronagraphs. C2 has a field of view (FOV) from 2.0 to 6.0 R_s, and COR1 from 1.5 to 4.0 R_s. Therefore, in Figure 6, we limit the FOV to 4.0 R_s. In each panel of Figure 6, the inner white dotted circle, the black solid circle, and the outer dashed white circle have radii of 1.0, 2.0, and 4.0 R_s, respectively. The color scale shows the relative changes in intensity of the WL total brightness with respect to the steady-state corona solar wind. Here we list our key findings by comparing the WL images, and propose possible explanations for some of them.

1. In the LASCO/C2 view, the core structure of the CME propagates eastward, as shown in Figures 6(a) and (b). The observation shows the CME to be symmetric along the equator, while the synthetic image shows the northern part of the CME to be brighter than the southern part. We examine the plasma properties in our simulations and find a high-density region ahead of the flux rope, which can slow down the CME propagation, thus contributing to this asymmetry (L. Zhao et al. 2024).
2. In the STA/COR1 view, we primarily see the traces of a structure propagating toward the far side of the Sun in Figures 6(c) and (d). The noisy white dots in the east part of the images may indicate the CME propagation direction; nonetheless, the changes in brightness are not very pronounced because of the separation in location, as shown in Table 2 and Figure 3(a). In our simulations, we basically reproduce these structures, including the propagation direction and some weakly intensified brightness in the east, as illustrated in Figure 6(d).
3. In the STB/COR1 view, the CME propagates westward with a nearly symmetric structure with respect to the solar equator. By comparing Figures 6(e) and (f), our model-synthesized WL image aligns with the observation except for some slight differences in the brightness in the south. This difference is likely related to the high-density region ahead of the flux rope in the simulation, which also affects the symmetry of the CME core structure from the point of view of LASCO/C2.

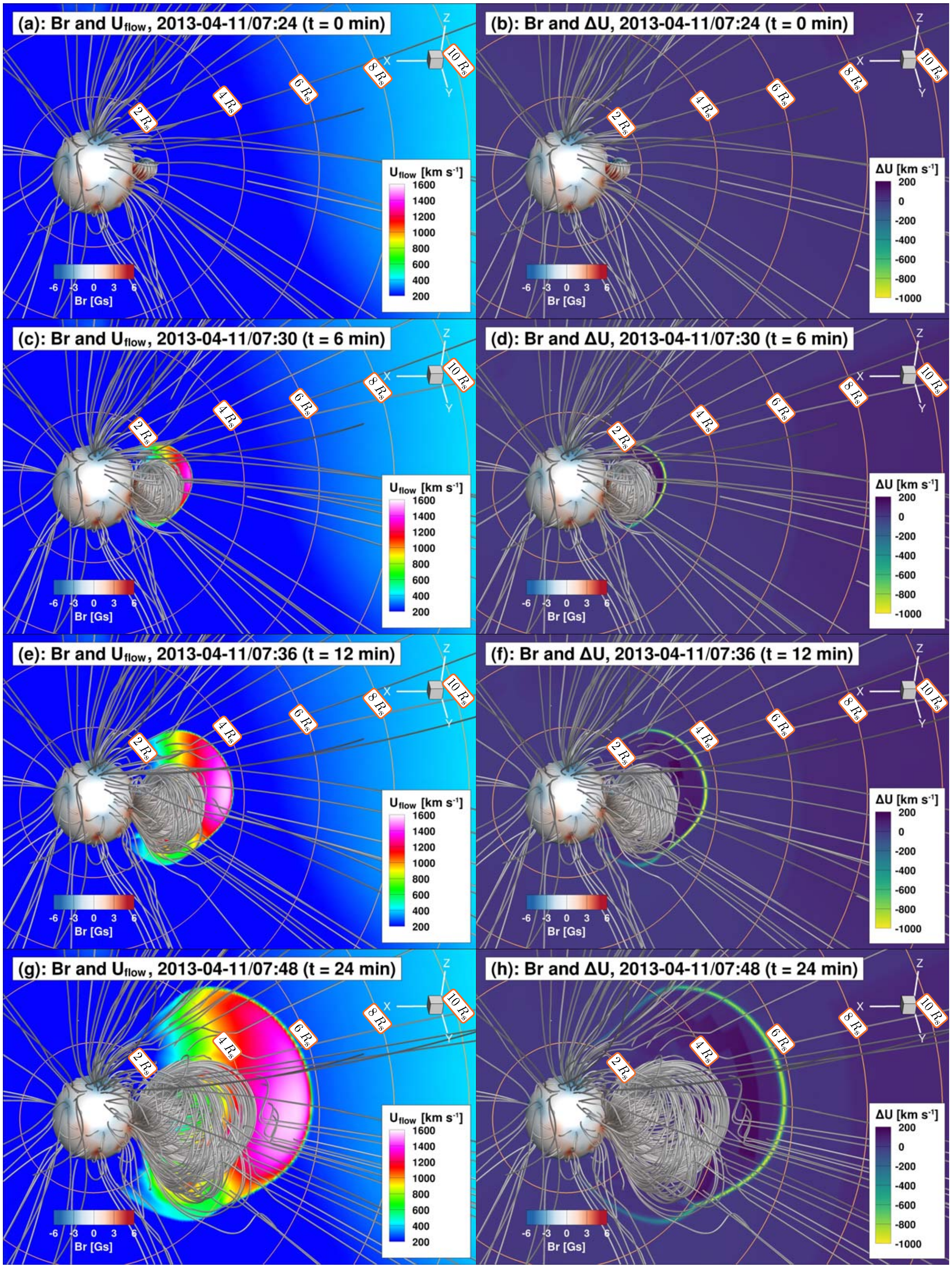

Figure 5. Evolution of the flux rope, the flow speed ($U_{\rm flow}$), and the $\Delta U = \Delta x \, \nabla \cdot \boldsymbol{u}$ value (divergence of the velocity field times the cell size) in the SC. In each panel, the 3D topology of multiple magnetic field lines is shown. The concentric circles represent the heliocentric distance in the contour slice, plotted every 2 $R_{\rm s}$ with the values written on each circle. HGR coordinates are used with the system rotated such that the negative X-axis points toward Earth. Panel (a) shows the initial flux rope at the solar surface with the radial magnetic field strength (B_r) plotted on the solar surface while the flow speed appears on the x–z plane in the SC. Panel (b) is similar to panel (a) but plotted with the ΔU value in the SC. Panels (c, d), (e, f), and (g, h) are similar to panels (a, b) but at 6, 12, and 24 minutes after the CME eruption, respectively.

Furthermore, we note that these images are influenced by significant projection effects, which can complicate the interpretation of the CME structure and brightness distribution (e.g., M. Temmer et al. 2009, 2023, and references therein).

4.3. Shock Wave Front

Because of the role played by CME-driven shocks in particle acceleration processes, CME-driven shock simulations are

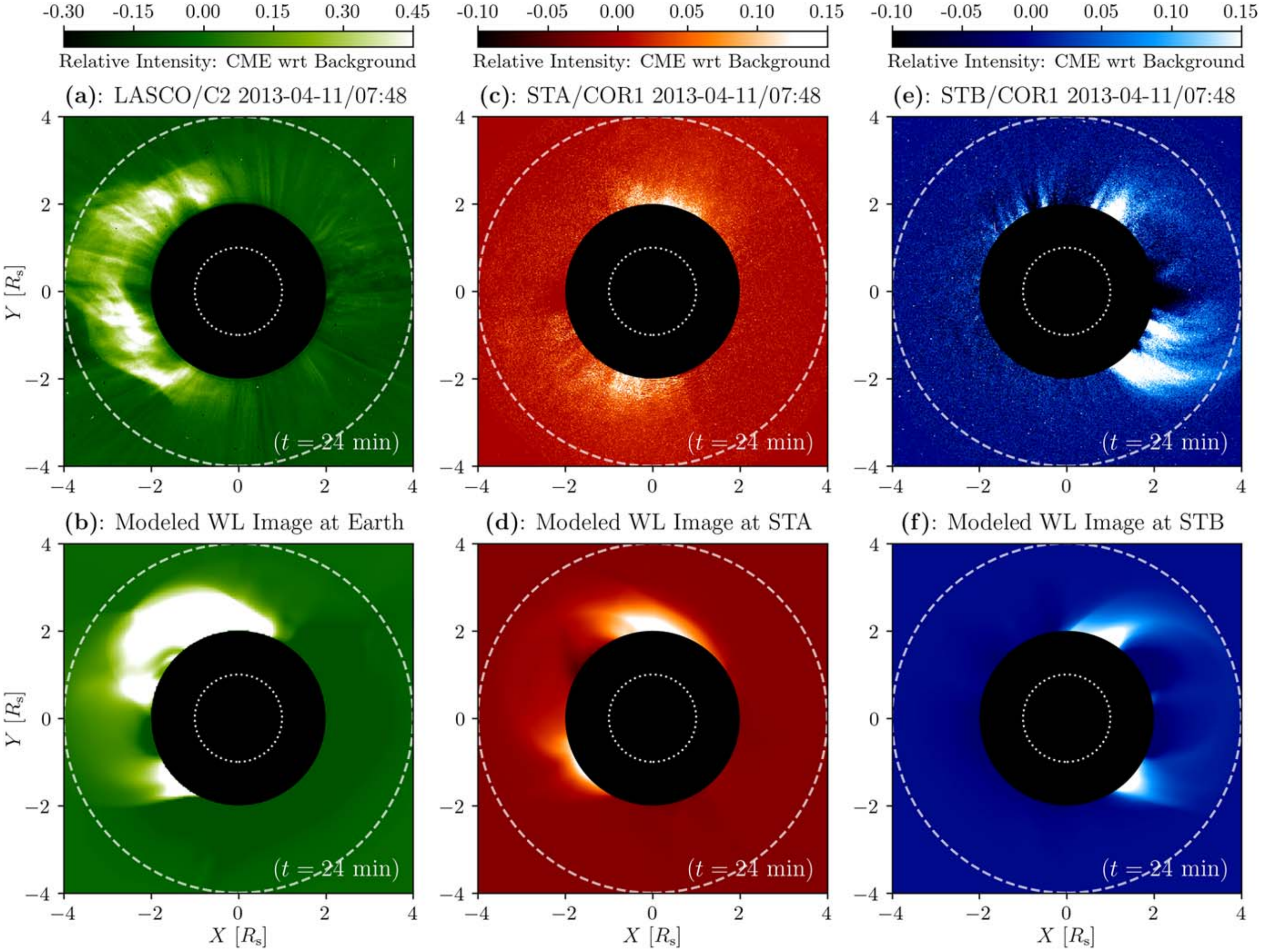

Figure 6. Comparison of the LASCO/C2 (left column), STA/COR1 (middle column), and STB/COR1 (right column) WL images at 24 minutes after the CME eruption. Upper panels are observations, and lower panels are the corresponding model-synthesized WL images. The color scale shows the relative changes in intensity of WL total brightness with respective to the solar wind before the eruption. In each image, the radii of the inner white dotted circle, the black solid circle, and the outer dashed white circle are $r = 1.0$, 2.0, and 4.0 R_s, respectively.

essential to calculate particle acceleration in the modeling of SEP events (e.g., Z. Mikić & M. Lee 2006; M. A. Lee et al. 2012; W. B. Manchester et al. 2017). Studies in the past have tried to reconstruct the shock surface and derive its properties, and they can be categorized into two broad types: (1) those using observational data such as EUV, WL coronagraphs and radio observations from which it is possible to infer the shock surface and its properties (e.g., V. Ontiveros & A. Vourlidas 2009; R.-Y. Kwon et al. 2014; A. P. Rouillard et al. 2016; I. Plotnikov et al. 2017; P. Zucca et al. 2018; A. Kouloumvakos et al. 2019; C. A. Maguire et al. 2020), and (2) those employing physics-based simulations to model the shock surface and its evolution (e.g., Z. Smith & M. Dryer 1990; D. Lario et al. 1998; F. Shen et al. 2011; T. Török et al. 2018; C. Downs et al. 2021; Z. Ding et al. 2022; M. Jin et al. 2022). While observational studies provide valuable constraints on shock properties, they are often limited by projection effects and assumptions about the applied shock geometry. On the other hand, simulations offer a more feasible way to study the evolution of shocks (e.g., W. B. Manchester et al. 2005). In our model, we develop a shock-capturing tool embedded in the MHD simulations, which enables shock identification with high spatial resolution in 3D and demonstrates the refined structure and complexity of the shock front, thus distinguishing it from many existing methods listed above.

In addition to the grid initialized as described in Section 2.1, in order to resolve the fine structures around the shock surfaces, the grid block resolution is refined by a factor of 2 at locations where the jump in ion thermal pressure between neighboring cells exceeds 2.0. Moreover, AWSoM-R incorporates a second-order shock-capturing scheme with slope limiters to enhance the accuracy of MHD parameters simulated near the shock front (G. Tóth et al. 2012; T. I. Gombosi et al. 2021).

In our model, $\Delta U = \Delta x \, \nabla \cdot \boldsymbol{u}$ is used as the criterion to extract the shock surface. The divergence of the velocity field is negative at the shock front and scales with the inverse of the shock width, which is proportional to the local mesh size Δx. In essence, ΔU indicates the jump in flow speed across one grid cell. In our shock-capturing tool, the shock surface is extracted along radial lines using a longitude–latitude grid with an angular resolution of $0^{\circ}\!.5$. Along each radial line, the shock wave front is identified by the smallest value of ΔU. Taking into account the fluctuations for the modeling tool and realistic structures in the system, a threshold of ΔU needs to be specified. This threshold is set as $\Delta U_t = -50\,\mathrm{km\,s^{-1}}$ by default. In our simulation, to better capture and visualize the shock, we set the threshold to be $\Delta U_{\rm t} = -120\,{\rm km\,s^{-1}}$. If the minimum ΔU is less than the threshold, the radial distance of the surface and the shock-associated parameters are saved; otherwise, the shock surface is not recognized.

Figure 7 shows the shock surface extracted at $t = 24$ minutes after the CME eruption from the front (left column) and back (right column) views. Here, the front view refers to the view from above AR 11719, and the back view is with a 180° rotation about the Z-axis. We show the shock wave front colored by the compression ratio, the shock angle, and the Mach number for the fast magnetosonic wave in panels (a, b), (c, d), and (e, f) of Figure 7, respectively. We can see that the 3D shock surface is nonuniform and consists of three spherical regions, due to the deformation of the flux rope in its interaction with the inhomogeneous background solar wind (see Figures 5(g, h)). Distinct variations in the shock properties can be found across small distances on the shock surface, especially near the interfaces of different spherical regions. Detailed calculations of the upstream shock normal, the shock angle, the shock speed, and the fast-mode Mach number are included in the Appendix.

The connection point of each observer on the shock surface is determined by tracing the magnetic field line from the location of the observer back to the shock surface in the 3D magnetic field solutions of AWSoM-R. Hereafter in this paper, when referring to the observer–shock front magnetic connection, we use the concept of "cobpoint", short for the *Connecting with the observerpoint*, which was first explicitly considered in modeling by A. Heras et al. (1995). In Figure 7, we show the field lines in the low solar corona at $t = 24$ minutes after the CME eruption, which connect to Earth, STA, and STB, plotted in green, pink, and orange, respectively. At $t = 24$ minutes, Earth and STB are magnetically connected to the shock, while STA is not. As illustrated in Figure 7, Earth is connected to the weak part of the shock with a compression ratio of about 1.5. The shock is quasi-parallel, with θ_{Bn} being about 30°, and the fast-mode Mach number is around 1.0. STB is connected to a stronger part of the shock with a compression ratio of about 2.0. θ_{Bn} is about 45°, indicating an oblique shock, and the fast-mode Mach number is around 2.0.

With a one-minute cadence, we trace the field lines and examine the shock properties at the cobpoint. Figure 8 illustrates the time evolution of the cobpoint properties corresponding to Earth and STB, plotted in green and orange, respectively. Properties of the STA-related cobpoint are not shown because STA is not magnetically connected to the shock. The properties displayed include the criterion we use to identify the shock surface (the ΔU value), the upstream flow speed ($U_{\rm flow}$), the shock speed ($U_{\rm shock}$), the fast-mode Mach number ($M_{\rm f}$), the shock angle (θ_{Bn}), and the density compression ratio ($\rho_{\rm down}/\rho_{\rm up}$)[20] from top to bottom panels in Figure 8. In Figure 8, it is shown that STB is magnetically connected to the shock surface around 5 minutes after the flux rope eruption, while Earth is connected to the shock surface around 15 minutes after the flux rope eruption. Moreover, STB is connected to a stronger shock in the first hour, whereas the shock to which the Earth is connected is very weak. Therefore, more effective particle acceleration is expected at the STB-connected shock than at Earth at the beginning of the event, explaining the fact that we see a more prompt onset at STB while the onset is more gradual at Earth, as shown in Figure 5 of D. Lario et al. (2014) with a zoomed-in time axis. Later, the shock region that Earth is connected to becomes slightly stronger than the one STB is connected to, with a higher compression ratio and higher fast-mode Mach number, as shown in Figures 8(d) and (f).

4.4. SEP Fluxes and Evolutions

In M-FLAMPA, 648 magnetic field lines are extracted and the distribution functions of energetic particles along each individual magnetic field line are solved. These 648 magnetic field lines are uniformly initialized on the $r = 2.5\,R_{\rm s}$ sphere that covers 360° in longitude and ±85° in latitude, as described in Section 2.3.3. Once the time-accurate simulation begins, that is, after the flux rope is placed on top of the AR, AWSoM-R and M-FLAMPA run concurrently. M-FLAMPA extracts the plasma parameters from AWSoM-R simulations every 2 minutes and calculates the acceleration and transport processes of particles. In the following sections, we show the simulation results and compare them with observations.

4.4.1. $Z = 0$ Plane Cut and Radial Distribution

Figure 9 shows a snapshot of simulation results in the solar equatorial plane where $Z_{\rm HGR} = 0$ as seen from above the north pole of the Sun, at 4 hr after the flux rope eruption. The magnetic field lines connecting to Earth, STA, and STB are plotted as green, pink, and orange curves, respectively. Discontinuities along the field lines within $\sim 20\,R_{\rm s}$, which connect to Earth and STB, can be found and are primarily due to the projection effect, the magnetic turbulence in downstream shock regions, as well as the flux rope interacting with the ambient solar wind plasma. Figures 9(a) and (b) show the plasma speed and ΔU (see Section 4.3). Panels (c) and (d) show the calculated differential intensity of protons at 2.4 and 22 MeV. Those two energy channels are chosen to compare with the SOHO and STB observations, as discussed below in Section 4.4.3. Since STA is not magnetically connected to the shock surface as seen in panels (a) and (b), and the perpendicular diffusion is not incorporated in this work, STA does not detect any particle enhancement. In addition, the longitudinal dependence of the particle intensity in panels (c) and (d) can be explained by the nonuniformity of the shock surface as seen in panels (a) and (b).

4.4.2. 2D Spherical Distribution

Figure 10 shows the two-dimensional (2D) distribution of the energetic proton differential intensity on a logarithmic scale at 4 hr (top row), 12 hr (middle row), and 36 hr (bottom row) after the launch of the CME flux rope. Two energy channels are shown, 2.4 MeV (left column) and 22 MeV (right column), corresponding to lower- and higher-energy protons. The x- and y-axes represent the HGR longitude and latitude on a sphere at 1 au. Earth, STA, and STB locations are marked by letters "E", "A", and "B" within green, pink, and orange circles, respectively. The location of the inserted flux rope on the Sun is marked as a blue square with the letter "F" showing the relative location of observers with respect to the flux rope (also see Figure 3(a)). A similar plot but for ⩾10 MeV integral flux

---

[20] Hereafter, $\langle \cdots \rangle_{\rm down}$ and $\langle \cdots \rangle_{\rm up}$ refer to the parameter downstream and upstream of the shock, respectively.

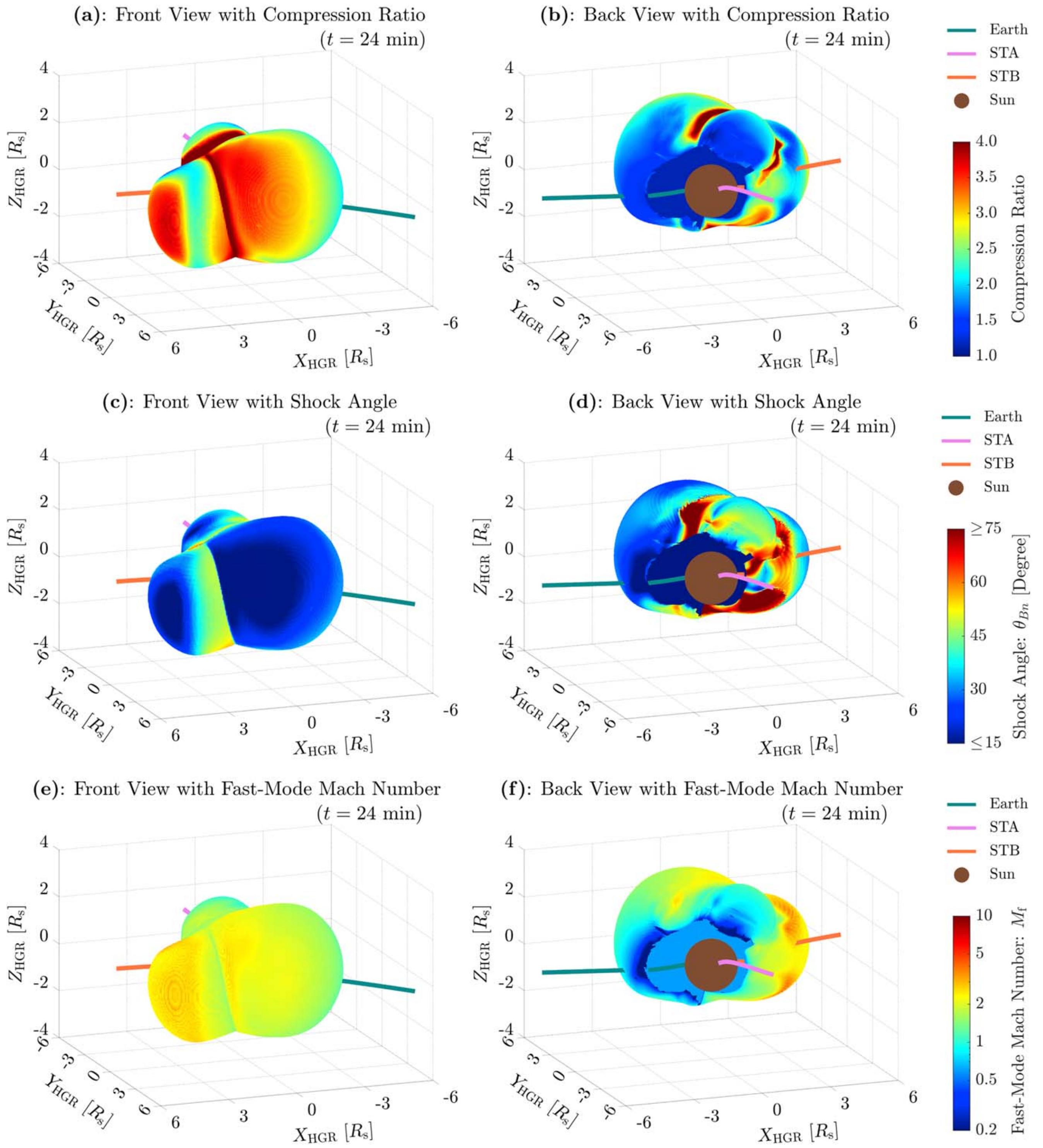

Figure 7. Extracted shock surface at 24 minutes after the flux rope eruption. HGR coordinates are used. In each panel, field lines connecting to Earth, STA, and STB are plotted in green, pink, and orange, respectively. The brown sphere in the center represents the Sun ($r = 1\ R_s$) in panels (b), (d), and (f). Panel (a) shows the front view of the shock surface colored with the shock compression ratio. The front view is defined as the view from above the AR. Panel (b) is similar to panel (a) but from the back view of the shock surface, which is rotated 180° about the Z-axis. Panels (c, d) and (e, f) are similar to panels (a, b) but colored with the shock angle (θ_{Bn}) and the fast-mode Mach number (M_f), respectively.

and with a different computational scheme is shown in Figure 5 of L. Zhao et al. (2024).

Note that the traced 648 magnetic field lines in M-FLAMPA are evenly distributed on the $2.5\,R_s$ sphere, but not evenly distributed over the sphere at 1 au because of the inhomogeneous magnetic fields in the simulation domain. Therefore, we apply the Delaunay triangulation method (B. Delaunay 1934; D.-T. Lee & B. J. Schachter 1980) to construct a skeleton of the sphere at 1 au, which uses a set of points to effectively divide the plane into multiple triangular cells and tends to avoid the formation of narrow or sliver triangles. In Figure 10, the vertices indicate where the field lines intersect with the 1 au

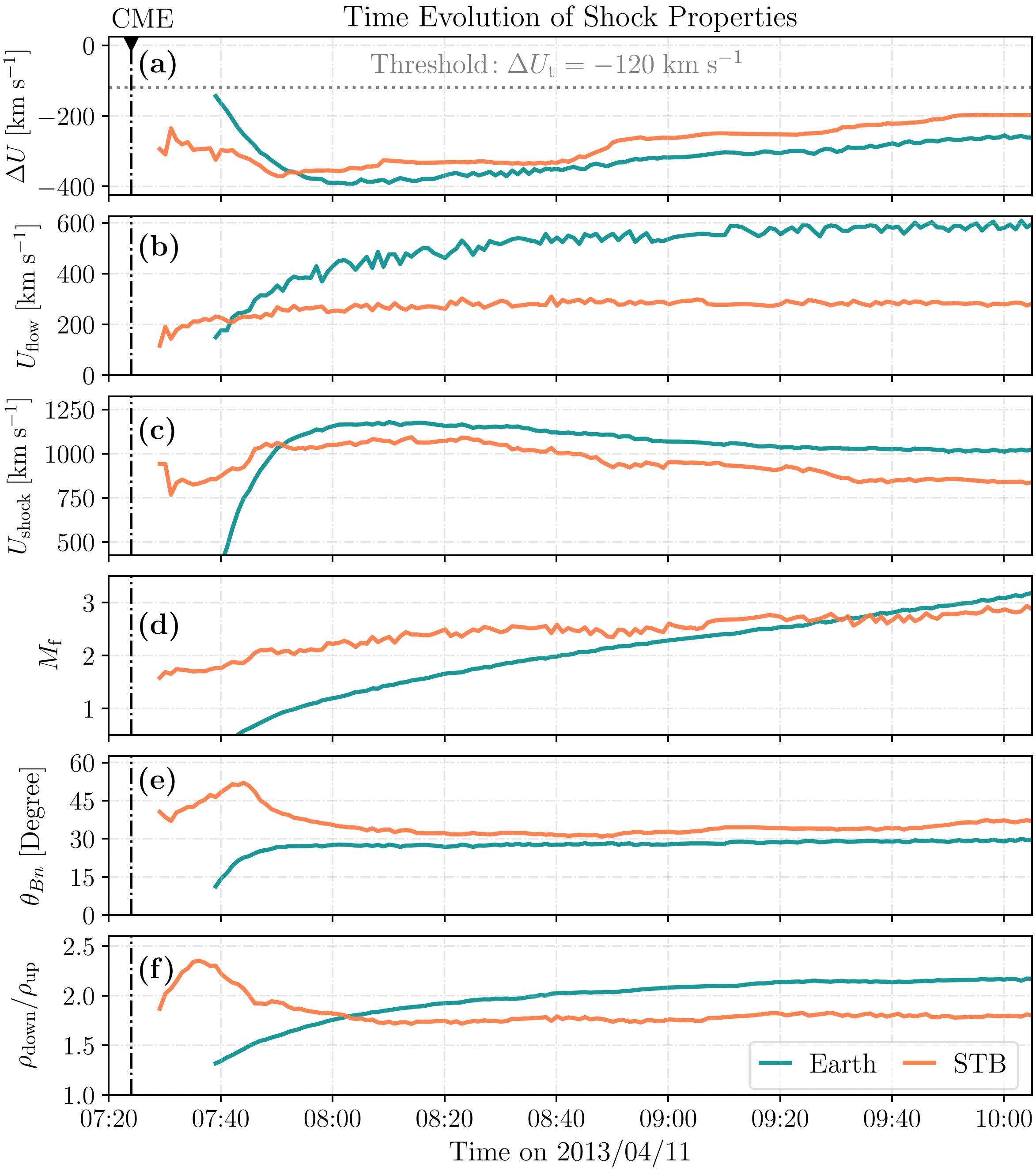

Figure 8. Time evolution of the shock properties at the intersection point of the shock surface with field lines connecting to Earth and STB, plotted in green and orange, respectively. Six parameters are presented from the top panel to the bottom: (a) The ΔU value, plotted with the gray dotted horizontal line for the shock identification threshold $\Delta U_t = -120$ km s^{-1} used in this study; (b): upstream solar wind speed (U_{flow}); (c) shock speed (U_{shock}); (d) fast-mode Mach number (M_f); (e) shock angle (θ_{Bn}); (f) density compression ratio ($\rho_{\mathrm{down}}/\rho_{\mathrm{up}}$). In each panel, a vertical dashed–dotted line represents the CME onset time.

sphere, and the edges illustrate the skeletal representation of the 1 au sphere derived via Delaunay triangulation. With the skeleton and differential intensity values at each vertex, we interpolate the intensity across the entire 1 au sphere. In each panel of Figure 10, the contours are plotted to show the structure of the distribution function.

Furthermore, comparing the distributions at energies of 2.4 MeV (left column) with 22 MeV (right column) in Figure 10, we see that the higher-energy protons generally arrive at the 1 au surface earlier than the lower-energy protons. We can also observe the phases of increase, peak, and decay for the differential intensity distribution at 2.4 MeV in Figures 10(a), (c), and (e).

Distinct variations in energetic proton intensities can also be found across longitudes and latitudes in Figure 10. For instance, in all three time slices (4, 12, and 36 hr after the flux rope eruption), the differential intensity around STA is orders of magnitude lower than that at Earth and STB, if any. This agrees with the observations in Figure 3 and is consistent with the simulation results shown in Figure 9, which shows no SEP fluxes in the regions near STA due to the lack of magnetic connectivity (see Section 4.3) and the absence of perpendicular

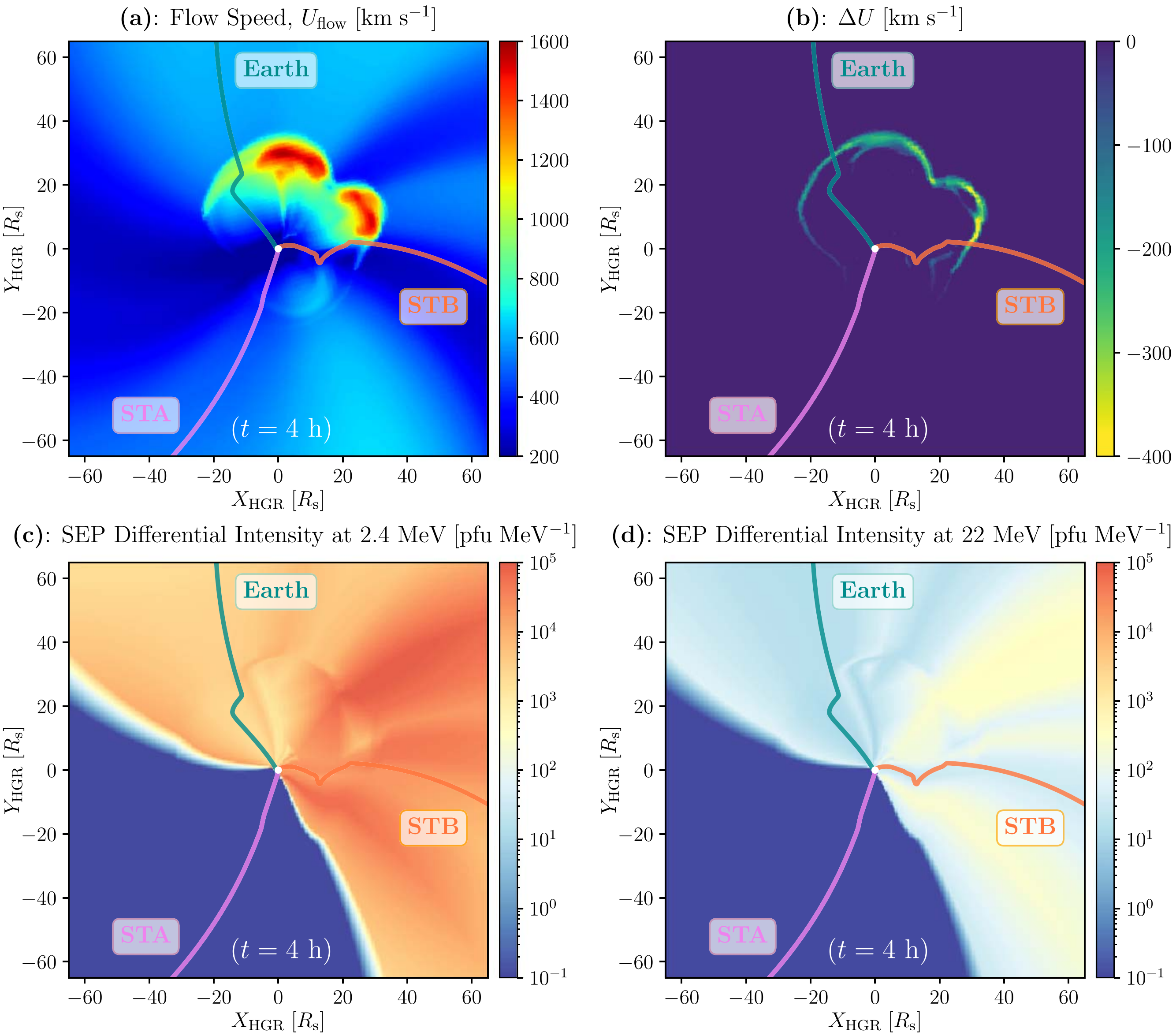

Figure 9. Simulation results in the solar equatorial plane ($Z_{\rm HGR} = 0$, viewed from the north pole of the Sun) at 4 hr after inserting the flux rope. In each panel, HGR coordinates are used, and the FOV is set as $-65\ R_s \leqslant X_{\rm HGR},\ Y_{\rm HGR} \leqslant 65\ R_s$. Field lines connecting to Earth, STA, and STB are plotted in green, pink, and orange, respectively, with corresponding labels next to the field lines. The white solid circle at the center represents the Sun (1 R_s). Panel (a) shows the flow speed. Panel (b) shows the ΔU value. Panels (c) and (d) show the energetic proton differential intensity at 2.4 and 22 MeV, respectively, with colors saturated if the intensity falls beyond the range from 10^{-1} to 10^5 pfu MeV^{-1}.

diffusion in our model. Hereafter, we focus on the particles observed at Earth and STB. Since the IMF follows the Parker spiral in general (e.g., H. Xie et al. 2019; L. Zhao et al. 2019), the SEP flux typically concentrates around 40°–80° east of the flux rope location, which also depends on the corona and IMF configurations (e.g., D. Lario et al. 2006; I. Richardson et al. 2014, 2018; M. Paassilta et al. 2018). As shown in Figures 10(b) and (c), the peak intensity at both energies occurs between 315° and 360° in our simulations, which is 70°–115° east of the flux rope location. Note that in our simulation, we assume a uniform injection coefficient throughout the shock front, that is, independent of the shock obliquity, as described in Section 2.3.5. Therefore, the 2D distribution of the energetic particles reflects the collective effects of the shock strength, as well as the ambient plasma density and temperature.

4.4.3. Time–Intensity Profiles

With the triangulation method described in Section 4.4.2, we interpolate the differential intensities at Earth and STB. Each panel of Figure 11 presents the calculated differential intensities across six energy channels, which we compare with particle measurements from SOHO/ERNE (panels (a, b)), and STB/LET and HET (panels (c, d)). These six energy channels for each spacecraft are chosen between ∼2 MeV and ∼40 MeV and are shown in different colors. In Figure 11, the simulation results using the Poisson bracket scheme are plotted as dashed lines, while the observational data are presented as solid lines. Overall, our model reproduces the time profiles across the six energy channels plotted for both SOHO and STB, with discrepancies within roughly half an order of magnitude. The

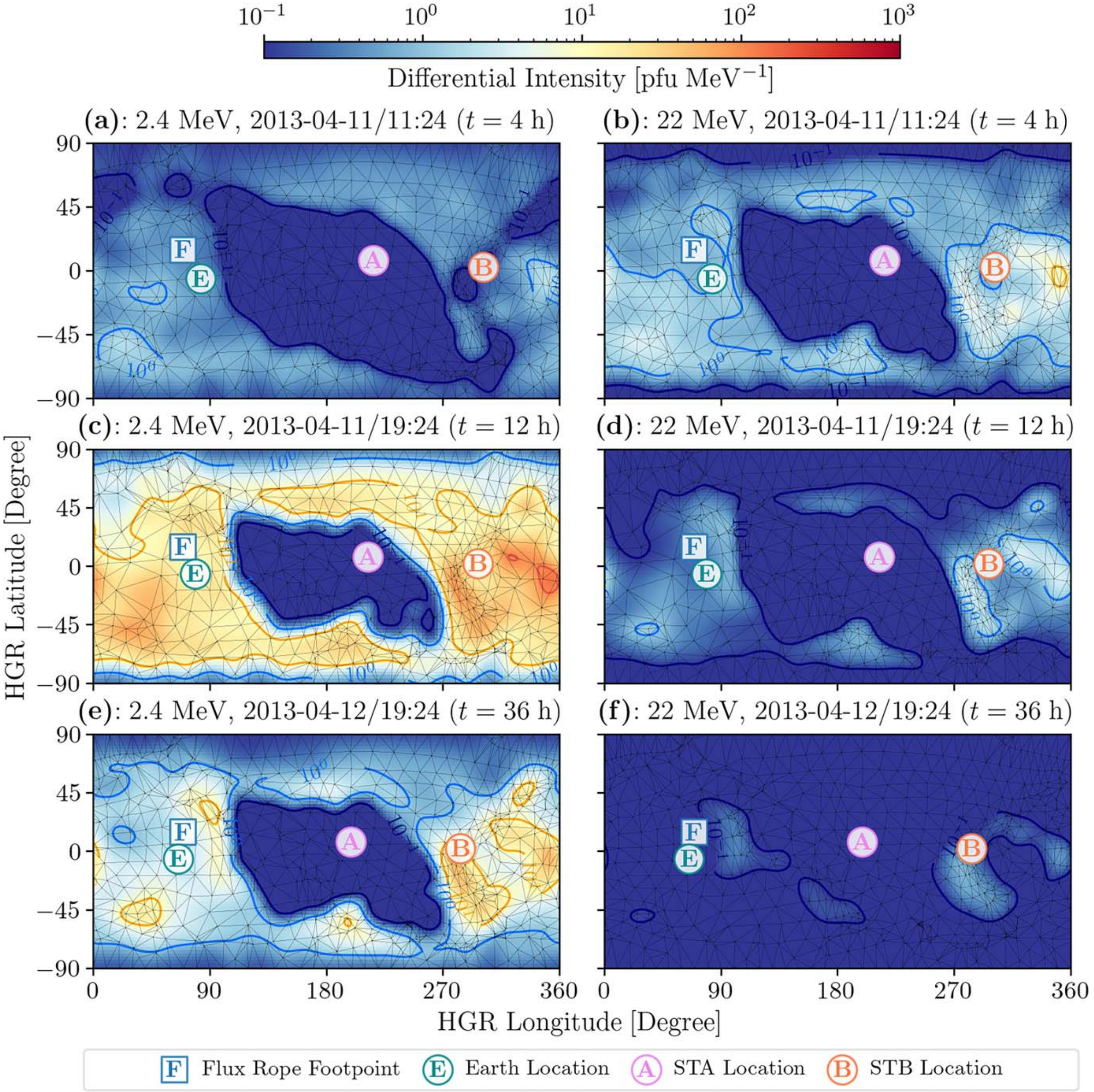

Figure 10. The 2D distribution of the energetic proton differential intensity at 2.4 MeV (left column) and 22 MeV (right column) on the 1 au sphere is shown at 4 hr (upper row), 12 hr (middle row), and 36 hr (lower row) after the CME eruption. In each panel, the *x*-axis and *y*-axis are the HGR longitude and latitude. The flux rope footpoint on the solar surface is marked as "F" in a square in blue, and the locations of Earth, STA, and STB are plotted as "E", "A", and "B" in circles in green, pink, and orange, respectively.

calculated intensities are slightly higher at STB with a faster decay phase than at Earth, as shown in Figures 11(a) and (c). Given that the scaling factor is set to be the same in the entire simulation domain, this discrepancy between STB and Earth is due to both the number of particles injected into the shock system and the different time-evolving shock properties at the cobpoint related to STB and Earth, as illustrated in Figures 7, 8, and 10.

In addition, for both SOHO and STB, a zoomed-in view in Figures 11(b) and (d) reveals that the onset times in the simulations agree with the observations in all six energy channels within two hours. A clear velocity dispersion is also shown at both locations. Specifically, for SOHO/ERNE, the onset phases are comparable between simulations and observations in the two intermediate-energy channels (8.0–10.0 and 13.0–16.0 MeV). However, in the two higher-energy channels (20.0–25.0 and 32.0–40.0 MeV), the SEP peak intensities arrive about 2 hr earlier in simulations than in observations. In the two lower-energy channels (2.0–2.5 and 4.0–5.0 MeV), the SEP peak intensities arrive slightly later in simulations than in observations. These differences may be due to the uncertainties in modeling the evolution of the Gibson–Low flux rope and the shock properties to which SOHO/ERNE is magnetically connected. More detailed discussions on the SEP onset and

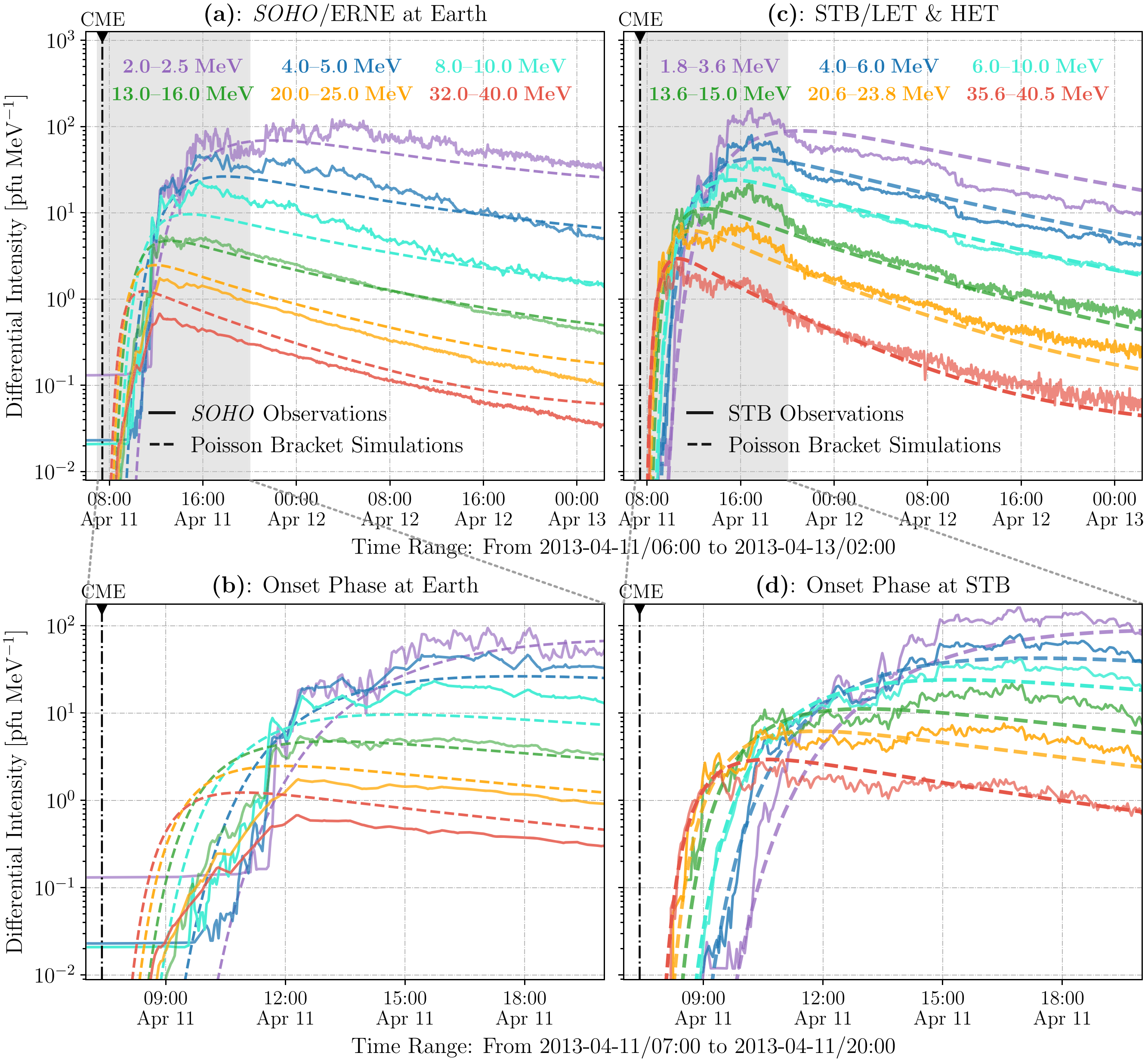

Figure 11. Comparison of the energetic proton time–intensity profiles between simulation results and observations across six energy channels that range from ∼2 MeV to ∼40 MeV. These energy channels, listed in panels (a) and (c), are chosen to match with each particle instrument and they are slightly different for each instrument. In each panel, the observations are plotted as solid curves, while the calculated intensities are plotted as dashed curves. A black dashed–dotted line represents the CME onset time. Panel (a) shows the comparison with SOHO/ERNE observations at Earth and panel (c) shows the comparison with STB/LET and HET in a window of ∼2days. The shaded regions in panels (a) and (c) mark the SEP onset phase during the first ∼12 hr, with corresponding zoomed-in time–intensity profiles shown in panels (b) and (d) over the same energy channels as those in panels (a) and (c), respectively. The ranges of *x*-axis and *y*-axis remain the same for panels in the same row.

peak timing and fluxes are provided along with results using different MFPs later in Section 4.4.5.

In terms of the time profiles in STB/LET and HET, there is an irregular structure in particle measurements around 17:00 UT on April 11 in Figure 11(c), which is not reproduced by the simulations. In addition to this short-term irregularity, the onset phases in simulations are comparable to those in observations across the six energy channels, except for the lower-energy channel (1.8–3.6 MeV), in which the calculated peak intensities are about 4 hr later than observed (see Figure 11(b)). Furthermore, the decay phases across all six energy channels for both SOHO and STB show a strong concordance between simulations and observations, within a factor of ∼2.

4.4.4. Energy Spectrum

Figures 12(a)–(c) depict the energy spectra at 4, 12, and 36 hr after the launch of the CME flux rope, respectively. In each panel, simulation results are plotted as curves, while observational data are shown as scattered points where the energy bin widths are indicated by horizontal bars. We subtract the background fluxes for all the particle measurements shown here. The SOHO/ERNE data are marked as green circles, and the simulated spectra at Earth are plotted as green lines. Note that the SOHO/ERNE data are subject to saturation effects, which may lead to inaccuracies in particle counts at high flux

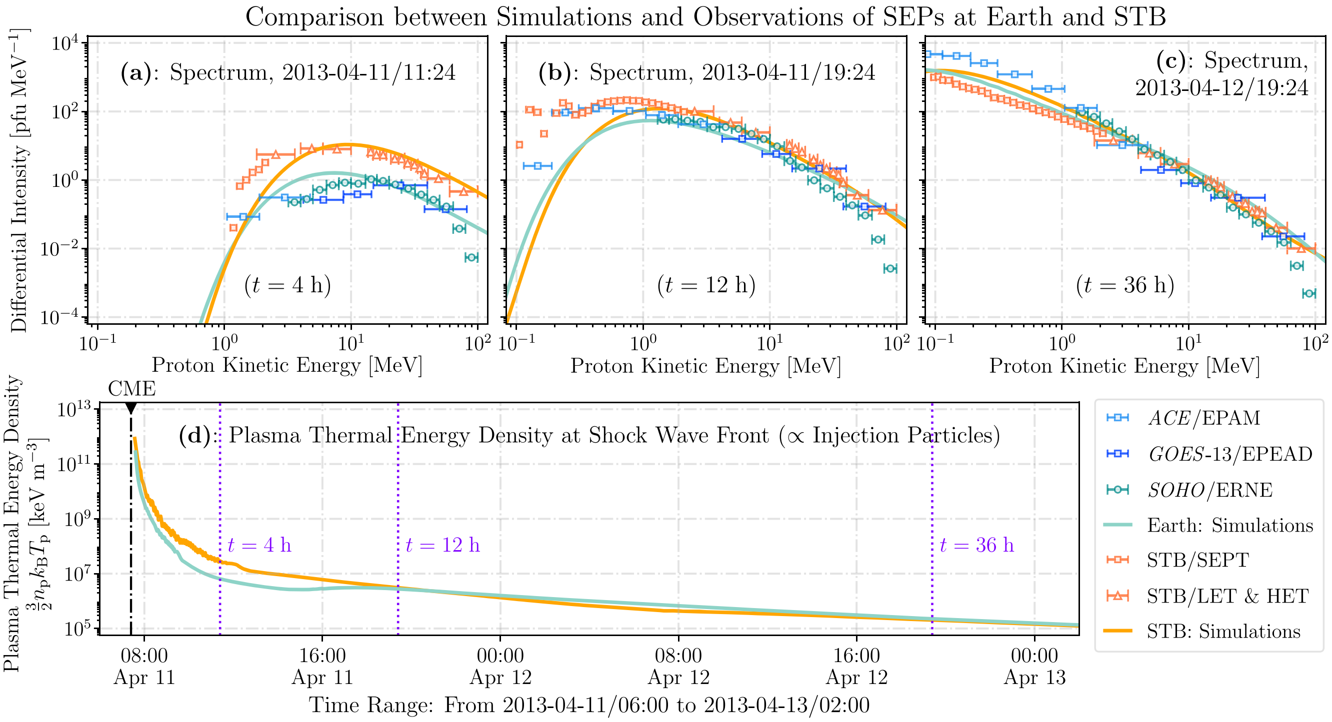

Figure 12. Comparison between simulations and observations of SEPs at Earth and STB. Panels (a)–(c) present the SEP spectra at Earth and STB at three time intervals after the CME flux rope eruption: (a) 4 hr, (b) 12 hr, and (c) 36 hr. In each panel, observational data are plotted as scattered points, while simulation results are shown as curves. Data from ACE/EPAM are plotted as light blue squares. Data from GOES-13/EPEAD are denoted by deep blue squares, with the so-called "effective energies" calibrated by A. Bruno (2017). Measurements from SOHO/ERNE are marked as green circles, and the simulated spectra at Earth are plotted in green. Similarly, orange squares represent data from STB/SEPT, orange triangles indicate data from STB/LET and HET instruments, and orange curves represent the simulated spectra at STB. Panel (d) shows the time profile of the ambient plasma thermal energy density at the shock wave front, using the same legends as in panels (a)–(c). Additionally, a black vertical dashed–dotted line represents the CME onset time, and three purple vertical dotted lines indicate the moments of 4, 12, and 36 hr after the CME eruption, respectively.

levels, especially at high energies (R. Miteva et al. 2018, 2020; P. Kühl & B. Heber 2019). Therefore, we also show particle measurements from the Energetic Proton, Electron and Alpha Detector (EPEAD, T. Onsager et al. 1996; F. B. Sellers & F. A. Hanser 1996) on board GOES-13, which are plotted as deep blue squares with energy bins calibrated by A. Bruno (2017). Measurements from STB/LET and HET instruments are marked as orange triangles, and the simulated spectra at STB are plotted as orange lines. At low-energy ranges, we include data from the Low-Energy Magnetic Spectrometer 120 (LEMS120) of the Electron, Proton, and Alpha Monitor (EPAM, R. E. Gold et al. 1998) on board ACE for near-Earth observations, and data from the Solar Electron and Proton Telescope (SEPT, R. Müller-Mellin et al. 2008) on board STB, marked as light blue squares and orange squares in Figure 12, respectively. Note that ACE/EPAM/LEMS120 does not distinguish between ion species, and we assume that its measured intensities are dominated by protons and that the contribution of heavier ions is small compared to that of protons (e.g., P. Marhavilas et al. 2015; D. Lario et al. 2018). STB/SEPT has four direction-dependent channels (sunward, antisunward, north, and south) and the observational data are averaged across these directional channels.

Overall, the simulation results are comparable to the particle measurements, particularly for energies above 1 MeV. Notably, the simulations capture the spectral shape during the onset phases and at later times with high fidelity. However, for low-energy protons, contamination from high-energy particles significantly impacts the ACE/EPAM/LEMS120 and STB/SEPT measurements, especially during the onset phase of SEP events (e.g., D. Haggerty et al. 2006; O. Malandraki et al. 2009; P. Marhavilas et al. 2015; B. Morgado et al. 2015; D. Lario et al. 2018; M. Brüdern et al. 2022, and references therein). As a result, only a limited number of energy channels in ACE/EPAM/LEMS120 and STB/SEPT provide valid measurements at $t = 4$ hr in Figure 12(a), and we also see a fluctuating spectrum observed by STB/SEPT at $t = 12$ hr in Figure 12(b). Furthermore, from the time–intensity profiles in Figure 11, we can find some short-term irregular structures at energies below 5 MeV in observations, which can also contribute to the differences in model–data comparison at low energies and at specific times in Figure 12. From the simulation perspective, the differences between the observed and simulated spectra at low energies (e.g., Figures 12(b) and (c)) underscore the challenges in completely accurate modeling of the acceleration and transport of low-energy particles.

Here, we discuss the spectrum differences between Earth and STB. In Figure 12(a), the particle intensity at STB is about half an order of magnitude higher than that at Earth, 4 hr after the flux rope eruption. The SEP intensities at these two locations become similar at later times, as illustrated in Figures 12(b) and (c). To explore these variations in SEP flux levels, we examine the time-evolving properties on the shock surface. According to Equation (21), the number of particles injected at the shock wave front is proportional to the ambient plasma thermal energy density (per volume), calculated as $\frac{3}{2}n_\mathrm{p}k_\mathrm{B}T_\mathrm{p}$. Figure 12(d) shows the time evolution of the plasma thermal energy at the shock wave front, with the same legends as those used in Figures 12(a)–(c). The black vertical dashed–dotted

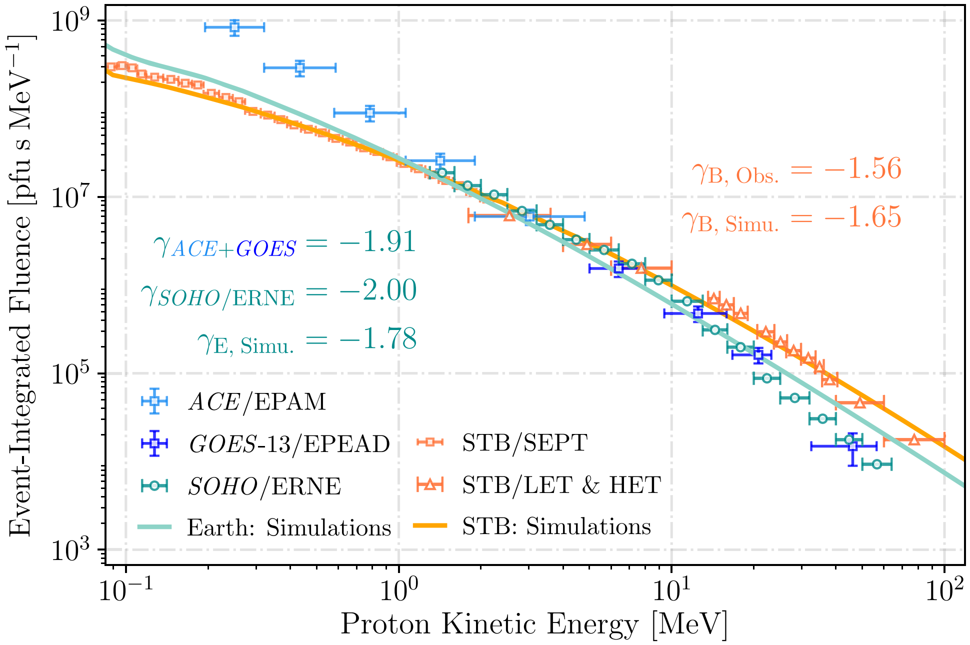

Figure 13. Event-integrated fluence spectrum at Earth and STB, with a similar legend style to that used in Figure 12 except for the vertical bars in the observational data, if shown, indicating the uncertainties of particle measurements. Fluence data from ACE/EPAM and GOES-13/EPEAD are taken from A. Bruno & I. G. Richardson (2021). Fitted spectral indices are included for both observations and simulations at Earth and STB in corresponding colors.

line marks the CME onset time and three purple vertical dotted lines indicate 4, 12, and 36 hr after the CME flux rope eruption, respectively. During the first few hours, the plasma thermal energy is slightly higher (by a factor of $\sim$3) at the cobpoint of STB than at Earth, due to the properties of the flux rope and ambient solar wind. Later, the plasma thermal energy is similar at the two cobpoints. This tendency contributes to the differences at earlier times and similarities at later times regarding the magnitude of SEP fluxes observed at Earth and STB shown in Figures 12(a)–(c). Since there is also a diffusion process, particle fluxes at later times are also affected by the earlier time to some extent.

To evaluate the overall event-integrated fluence, we calculate the SEP intensities over time across multiple energy channels, as illustrated in Figure 13. The SEP intensities are integrated in the first three days of this event. Consistency of the fluence intensity and spectral shape can be found in Figure 13, especially for the fluence spectrum at STB and the part of 1 MeV at Earth. We also calculate the spectral index of the fluence spectrum in the energy range from 1.0 to 50 MeV for both simulations and observations at Earth and STB. The spectral indices from simulations are consistent with the ones derived from observations. A slightly harder fluence spectrum at STB ($\gamma_{\mathrm{B,Simu}} = -1.65$) than at Earth ($\gamma_{\mathrm{E,Simu}} = -1.78$) is reproduced from our simulations.

In spite of the good agreement in model–data comparisons, we can discern noticeable differences at energies $\lesssim$1 MeV between simulations and observations in both time-evolving spectra shown in Figures 12(a)–(c) and fluence spectra shown in Figure 13. As discussed in the text associated with Figure 12, these differences between simulated and observed spectra arise from a combination of factors, including the background solar wind, CME propagation, shock properties, particle acceleration and transport processes, as well as the instrumental effects and some short-period irregularities at low energies (also see Figure 11). Next, we will discuss how the MFP affects the particle acceleration and transport processes in simulations.

4.4.5. Influence of MFPs on SEP Acceleration and Transport

Based on the DSA mechanism, the diffusion coefficient plays a critical role in the acceleration and transport processes of energetic particles. In M-FLAMPA, only the parallel diffusion and MFP are considered (see Section 2.3.2). In the following, we further investigate and discuss the influence of the parallel MFP estimation, which is derived from quasi-linear theory but manipulated differently in the upstream and downstream shock regions (see more details in Section 2.3.4).

In Figure 14, we plot $\lambda_{\|}$ for 10 keV injected protons at 4 hr after the CME eruption. Figure 14(a) shows $\lambda_{\|}$ calculated using Equation (18) in the equatorial plane, plotted with the shock front, the magnetic field lines connecting to Earth, STA, and STB, as well as the cobpoints related to Earth and STB. In Figure 14(a), the regions with a dramatic increase in $\lambda_{\|}$ correspond to the disruptions caused by the flux rope in the background solar wind, and the regions with smaller $\lambda_{\|}$ ahead of the flux rope are where the particles are accelerated effectively. In Figure 14(b), we plot $\lambda_{\|}$ at the injection energy of 10 keV for protons, derived from Equations (14) and (17), and calculated by Equations (15) and (18) along the field lines connecting to Earth, STA, and STB. In the region far upstream of the shock, i.e., in the background solar wind, we can see reasonably good agreement using these different approaches.

Note that in the upstream region, the free parameter λ_0 in Equation (15) is chosen to be 0.3 au in order to match $D_{\|}$ based on long-term PSP observations of solar wind turbulence (X. Chen et al. 2024), as shown in Figure 2. Even though the results in Figure 2 are overall consistent, there are still discrepancies for $D_{\|}$, especially at a small heliocentric distance. For long-term observations of solar wind magnetic field turbulence, although the results of X. Chen et al. (2024) are

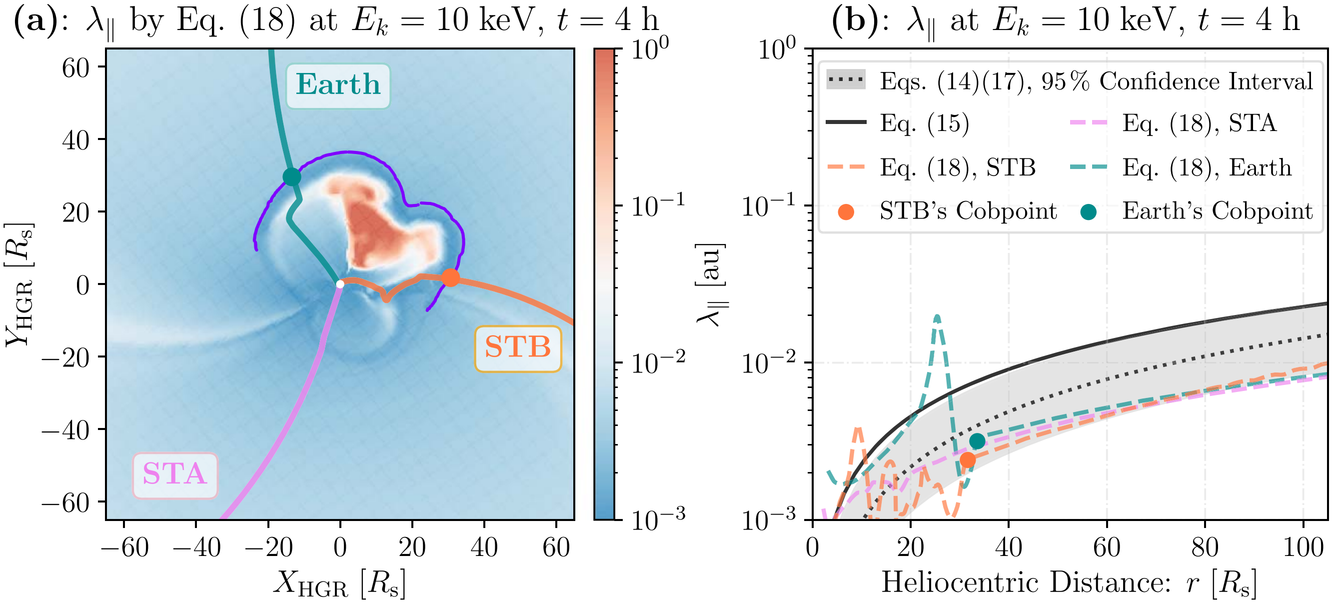

Figure 14. The parallel MFP ($\lambda_\parallel$) for the injected protons at 10 keV, 4 hr after the CME flux rope eruption. (a) $\lambda_\parallel$ in the solar equatorial plane ($Z_{\rm HGR} = 0$, viewed from the north pole of the Sun) using magnetic field turbulence modeled by AWSoM-R and following Equation (18). The contour colors saturate for $\lambda_\parallel$ values beyond the range from 10^{-3} to 10^0 au. In panel (a), HGR coordinates are used, with the FOV spanning $-65\ R_s \leqslant X_{\rm HGR}, Y_{\rm HGR} \leqslant 65\ R_s$. The white spot in the center represents the Sun (1 R_s). The shock front identified by the shock-capturing tool (see Section 4.3 and Figure 9(b)) is indicated by the purple markers. Magnetic field lines connecting to Earth, STA, and STB are plotted in green, pink, and orange, respectively. (b) The comparison of $\lambda_\parallel$ for 10 keV protons as a function of heliocentric distance. The black dotted curve corresponds to $\lambda_\parallel$ derived from Equations (14) and (17) with the gray shaded region indicating the 95% confidence interval. The black solid curve indicates $\lambda_\parallel$ calculated by Equation (15), while the dashed curves represent $\lambda_\parallel$ calculated by Equation (18) using time-accurate AWSoM-R parameters, plotted in the corresponding colors for each spacecraft as used in panel (a). Cobpoints associated with Earth and STB are shown in both panels. The color bar axis in panel (a) and the y-axis of panel (b) share the same label tag.

comparable to previous studies such as X. Moussas et al. (1992) and G. Erdős & A. Balogh (2005), there are still various factors that can influence the strength of background turbulence and the estimation of $D_\parallel$, such as the IP transients (e.g., M. Desai & J. Giacalone 2016; A. Pitňa et al. 2021, and references therein) and switchbacks (e.g., T. D. de Wit et al. 2020; M. Shoda et al. 2021). As a result, the optimal value λ_0 for the upstream MFP may vary from event to event in modeling historical SEP events.

For this event, we also explore the variations in SEP time–intensity profiles and fluence spectra caused by different values of λ_0. We set λ_0 in Equation (15) to be 0.1, 0.3, and 1.0 au, and present the time–intensity profiles and fluence spectra for both Earth and STB in Figure 15. Panels (a) and (d) show the time–intensity profiles for low-energy protons, with 2.0–2.5 MeV from SOHO/ERNE and 1.8–3.6 MeV from STB/LET. Panels (b) and (e) correspond to the high-energy proton profiles, featuring 20.0–25.0 MeV in SOHO/ERNE and 20.6–23.8 MeV in STB/HET. The fluence spectra and the fitted spectral indices are shown in panels (c) and (f) for Earth and STB, respectively.

The SEP time–intensity profiles in Figures 15(a), (b), (d), and (e) show that not only the absolute flux level, but also the onset and decay phases are sensitive to the MFP. Similarly, simulation results in Figures 15(c) and (f) demonstrate that different MFPs lead to a softer or harder fluence spectrum at lower- and higher-energy ends. While the simulations with $\lambda_0 = 0.3$ au achieve the best agreement with the observed time–intensity profiles, discrepancies still remain in the spectral index compared to observations at both Earth and STB. These comparisons show the influence of the fine-tuned upstream MFP parameter for this event in our model and also highlight the significance with respect to the transport process of SEPs. In fact, the transport of SEPs in the IP medium involves a range of different physical processes, including magnetic focusing, adiabatic cooling, drift, and parallel and perpendicular diffusion (T. G. Northrop 1963; E. Roelof 1969; J. Skilling 1971; J. Kóta 1997; P. Prinsloo et al. 2019; Y. Wang & J. Guo 2024). All of these processes depend intricately on the properties of the solar wind plasma and magnetic fields. The magnetic turbulence in the solar wind, for example, can influence the timing of the first arriving particles, the timing when the particle flux crosses a preset threshold (e.g., G. Qin et al. 2005; Y. Wang & G. Qin 2015), and also the event-integrated energy spectral index (e.g., L. Zhao et al. 2016, 2017). Discrepancies in model–data comparisons as shown in Sections 4.4.3–4.4.5 are consequences of the physical processes of SEPs mentioned above, as well as the uncertainties in modeling the properties of the background solar wind, the CME flux rope, and the shock.

5. Summary and Conclusions

As SEPs can pose significant radiation hazards in space, it is crucial to understand their underlying physics including the particle acceleration and transport processes. Achieving this understanding requires not only a comprehensive analysis of observed SEP events but also the development of models and tools capable of capturing these complex processes for SEPs. In this work, we focus on the methodological advancements by developing a shock-capturing tool and implementing the Poisson bracket into the SWMF/SOFIE. To demonstrate the capability of the model development, we utilize them to investigate a historical SEP event on 2013 April 11, which is characterized by the absence of significant SEP fluxes at STA and faster SEP onset at STB than at Earth.

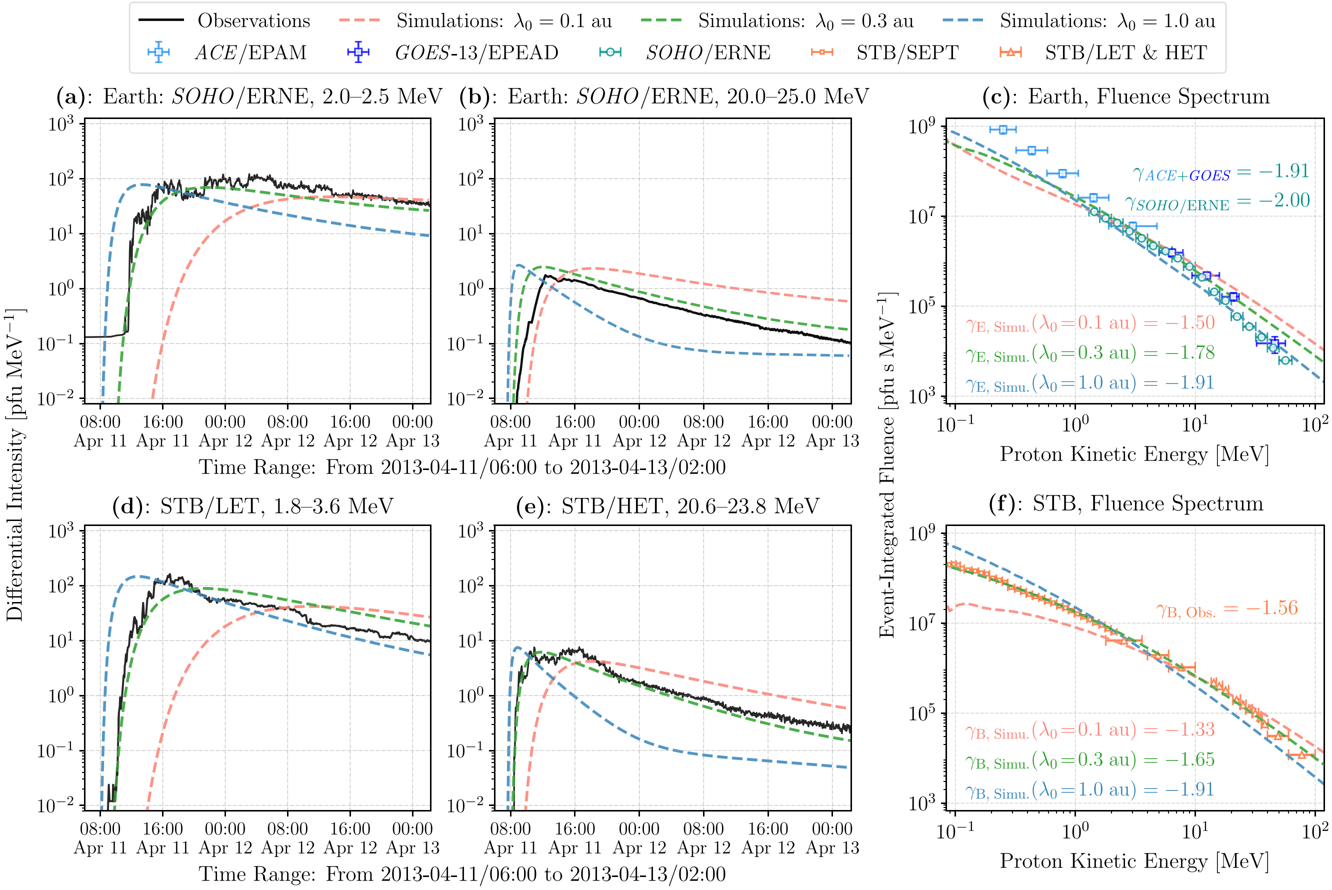

Figure 15. Calculated time–intensity profiles and energy spectra with different MFPs. (a), (b) The SEP time–intensity profiles at Earth in the energy ranges 2.0–2.5 MeV and 20.0–25.0 MeV, representing comparatively lower and higher energies, respectively. (c) Comparison of fluence spectra at Earth. (d), (e) The SEP time–intensity profiles at STB in the energy ranges 1.8–3.6 MeV and 20.6–23.8 MeV, corresponding to comparatively lower and higher energies, respectively. (f) Comparison of fluence spectra at STB. In each panel, simulation results are shown for three different MFP values, with λ_0 in Equation (15) set to 0.1, 0.3, and 1.0 au, represented as red, green, and blue dashed curves, respectively. Observational data are plotted as solid black lines for time series in panels (a), (b), (d), and (e), and marked as scattered points for the fluence spectrum in panels (c) and (f). The observational data in panels (c) and (f) follow the same legend style as used in Figure 13. Fitted spectral indices of the fluence spectrum are included for both observations and simulations using different MFPs at Earth and STB, displayed in the corresponding colors for the λ_0 value.

Our study begins with steady-state solar wind simulations driven by the stream-aligned AWSoM-R model, using the hourly updated GONG magnetogram. The simulations yield reasonable solar wind solutions, which show the magnetic field aligned with solar wind plasma streams and are validated against multipoint EUV observations shown in Figure 4. Although the small-scale structures on the solar surface are not fully captured, the steady-state solutions show reasonably well open fluxes from the CHs and good agreement for the average brightness, scales, and locations of large-scale structures. These solar wind solutions establish a suitable background through which the CME and SEPs propagate.

We then simulate the CME by placing a force-imbalanced GL flux rope with EEGGL-derived magnetic configurations within the source AR. The propagation of the CME flux rope is validated through the WL image comparisons (see Figure 6) with multipoint observations from SDO/AIA as well as COR1 on board STA and STB. As the CME propagates into the SC and IH domains, it interacts with the ambient solar wind, producing fast-mode shock fronts where particles are accelerated effectively. A shock-capturing tool has been developed to study the properties of CME-driven shocks starting from the low solar corona. Using the AMR technique and the criterion for the jump in speed (ΔU value), our shock-capturing tool shows the complex shock dynamics with high spatial resolution. The shock surface extracted using the shock-capturing tool is not only asymmetric and nonuniform but also consists of three spheres (see Figure 7), primarily due to the properties of the nonuniform solar wind in the solar corona and the deformation of the flux rope.

After identifying the shock front, we find that there is no magnetic connectivity to the shock for STA during this event, accounting for the absence of noticeable enhancements in SEP intensity at STA. Moreover, we plot the time-evolving shock properties in Figure 8, demonstrating that the magnetic connectivity to the shock wave front is established earlier for STB than for Earth, along with a higher compression ratio at the onset phase. Our simulation results about the shock help us to understand how this complex shock surface affects the particle acceleration process and explain the observed differences of SEP behaviors, further underscoring the versatility and potential of the shock-capturing tool for simulating intricate CMEs.

In order to accurately solve the kinetic equation governing the acceleration and transport processes of energetic particles, we have implemented the I. V. Sokolov et al. (2023) Poisson bracket scheme, which conserves the particle number and maintains the TVD property, into SOFIE/M-FLAMPA. We describe the formulation of the governing equation, the implementation of the scheme, and the setup of the free parameters in detail. Then, we show varieties of synthetic observables, including the SEP fluxes in plane cut, 2D particle intensity distribution in longitude and latitude on the 1 au sphere, time–intensity profiles, and energy spectra, showcasing the integration of the Poisson bracket scheme and also providing insights into understanding the SEP behaviors. Moreover, we present the effects of the parallel MFP on the SEP time–intensity profiles and fluence spectra by choosing different upstream MFP parameters. Differences between the simulations and particle measurements arise from a combination of the instrumental effects, short-period structures, and uncertainties in modeling the background solar wind, CME propagation, shock properties, magnetic connectivity, and particle acceleration and transport processes.

In summary, this study represents an advancement of SWMF/SOFIE in SEP modeling by integrating newly developed methodologies and demonstrating their applications. The implementation of the Poisson bracket scheme within the SWMF enables high-resolution simulations for SEPs, and the shock-capturing tool facilitates understanding how the shock properties affect the particle acceleration process. These methodological developments, combined with a variety of synthetic observables, facilitate the elucidation of the underlying physics during the 2013 April 11 SEP event, enhancing our knowledge of the acceleration and transport processes of SEPs.

Acknowledgments

The authors sincerely thank the anonymous reviewer for the time and effort devoted to improving this paper. This work is supported by NASA Living With a Star (LWS) Strategic Capability project under NASA grant 80NSSC22K0892 (SCEPTER), NASA Space Weather Center of Excellence program under award 80NSSC23M0191 (CLEAR), NASA grant 80NSSC21K1124, NSF ANSWERS grant GEO-2149771 and NASA LWS grant 80NSSC20K1778. Dr. Bruno also acknowledges support by NASA under award 80GSFC24M0006. The authors express their great gratitude to the SOHO project, an international cooperation between ESA and NASA, and to the SDO, STEREO, ACE, GOES, and PSP teams. The authors acknowledge the development of StereoCAT (see footnote 12) for CME analysis, as well as the DONKI (see footnote 13), CDAW (see footnote 14), and OMNI (see footnote 17) data sets. The authors also thank the Virtual Solar Observatory (VSO, see footnote 19) project at the National Solar Observatory (NSO), which serves as a research tool allowing scientists to search for the solar and heliospheric physics data. This work utilizes data from the NSO Integrated Synoptic Program, which is operated by the Association of Universities for Research in Astronomy, under a cooperative agreement with the National Science Foundation and with additional financial support from the National Oceanic and Atmospheric Administration, the National Aeronautics and Space Administration and the United States Air Force. The GONG (see footnote 10) network of instruments is hosted by the Big Bear Solar Observatory (USA), High Altitude Observatory (USA), Learmonth Solar Observatory (Australia), Udaipur Solar Observatory (India), Instituto de Astrofisica de Canarias (Spain), and Cerro Tololo Inter-American Observatory (Chile). Computational resources supporting this work are provided by the NASA High-End Computing (HEC) Program[21] through the NASA Advanced Supercomputing (NAS) Division at the Ames Research Center. Any opinions, findings, conclusions or recommendations expressed in this material are those of the authors and do not necessarily reflect the views of the National Aeronautics and Space Administration.

Appendix
Shock Formulation

A.1. Shock Normal and Shock Angle

As the shock wave front is captured, the direction of the normal to the front, $\hat{\boldsymbol{n}}$, can be found using the continuity of the normal component of the magnetic field (e.g., Equation (5.86) in J. D. Jackson 1998) upstream and downstream:

$$(\boldsymbol{B}_{\rm down} - \boldsymbol{B}_{\rm up}) \cdot \hat{\boldsymbol{n}} = 0. \tag{A1}$$

As far as it concerns the tangential components ($\boldsymbol{B}_t$) of the magnetic field upstream and downstream, the Rankine–Hugoniot relationships (W. J. M. Rankine 1870; H. Hugoniot 1889a, 1889b) as applied to MHD dictate that $\boldsymbol{B}_{t,\rm up}$ and $\boldsymbol{B}_{t,\rm down}$ are aligned with the jump in the tangential component of the plasma bulk velocity, $(\boldsymbol{u}_{\rm down} - \boldsymbol{u}_{\rm up})_t$, in the MHD shock waves (see, e.g., the introductory part of Chapter 72 of L. D. Landau et al. 2013), giving

$$\begin{aligned}&(\boldsymbol{u}_{\rm down} - \boldsymbol{u}_{\rm up})_t \parallel \boldsymbol{B}_{t,\rm up} \parallel \boldsymbol{B}_{t,\rm down}\\ &\parallel (\boldsymbol{B}_{\rm down} - \boldsymbol{B}_{\rm up})_t \;\equiv\; (\boldsymbol{B}_{\rm down} - \boldsymbol{B}_{\rm up}),\end{aligned} \tag{A2}$$

where the last identity accounts for Equation (A1) to express the alignment direction in terms of the easy-to-calculate difference in the magnetic field (see also R. Lepping & P. Argentiero 1971; B. Abraham-Shrauner 1972). Thus, eliminating the projection of the velocity jump, $\boldsymbol{u}_{\rm down} - \boldsymbol{u}_{\rm up}$, onto the direction of $\boldsymbol{B}_{\rm down} - \boldsymbol{B}_{\rm up}$ gives the jump in the normal velocity:

$$\begin{aligned}&(\boldsymbol{u}_{\rm down} - \boldsymbol{u}_{\rm up})_n\\ &= \begin{cases} \boldsymbol{u}_{\rm down} - \boldsymbol{u}_{\rm up}, & \boldsymbol{B}_{\rm down} = \boldsymbol{B}_{\rm up},\\ \dfrac{[(\boldsymbol{B}_{\rm down} - \boldsymbol{B}_{\rm up}) \times (\boldsymbol{u}_{\rm down} - \boldsymbol{u}_{\rm up})] \times (\boldsymbol{B}_{\rm down} - \boldsymbol{B}_{\rm up})}{(\boldsymbol{B}_{\rm down} - \boldsymbol{B}_{\rm up})^2}, & \boldsymbol{B}_{\rm down} \neq \boldsymbol{B}_{\rm up}. \end{cases}\end{aligned} \tag{A3}$$

Finally, the direction of the unit normal to the front pointing from downstream of the shock to upstream is given by

$$\hat{\boldsymbol{n}} = \frac{(\boldsymbol{u}_{\rm down} - \boldsymbol{u}_{\rm up})_n}{|(\boldsymbol{u}_{\rm down} - \boldsymbol{u}_{\rm up})_n|}. \tag{A4}$$

The upstream shock angle, θ_{Bn}, can be derived by measuring the angle between the upstream magnetic field and the shock normal (see more analysis by, e.g., J. Chao & K. Hsieh 1984):

$$\theta_{Bn} = \arccos\frac{|\boldsymbol{B}_{\rm up} \cdot \hat{\boldsymbol{n}}|}{|\boldsymbol{B}_{\rm up}|}. \tag{A5}$$

A.2. Shock Speed and Fast-mode Mach Number

Based on the equation of continuity (e.g., Chapter 1 of L. D. Landau & E. M. Lifshitz 1987), the mass flux remains

---

[21] https://www.nas.nasa.gov/hecc/

continuous across the shock front:

$$\rho_{\mathrm{down}}(U_{n,\,\mathrm{down}} - U_{\mathrm{shock}}) = \rho_{\mathrm{up}}(U_{\mathrm{shock}} - U_{n,\,\mathrm{up}}). \tag{A6}$$

Here, U_{shock} denotes the shock speed, and $U_{n,\,\mathrm{down}} = \boldsymbol{u}_{\mathrm{down}} \cdot \hat{\boldsymbol{n}}$ and $U_{n,\,\mathrm{up}} = \boldsymbol{u}_{\mathrm{up}} \cdot \hat{\boldsymbol{n}}$ represent the downstream and upstream flow speeds normal to the shock, respectively. The shock speed is then given as

$$U_{\mathrm{shock}} = \frac{\rho_{\mathrm{down}} U_{n,\,\mathrm{down}} - \rho_{\mathrm{up}} U_{n,\,\mathrm{up}}}{\rho_{\mathrm{down}} - \rho_{\mathrm{up}}}, \tag{A7}$$

as commonly employed in previous studies (e.g., Y. Whang et al. 1996; Z. Ding et al. 2022; M. Jin et al. 2022, and references therein). With the shock normal in Equation (A4), the shock velocity can be expressed as

$$\boldsymbol{U}_{\mathrm{shock}} = U_{\mathrm{shock}}\,\hat{\boldsymbol{n}}. \tag{A8}$$

Then, we calculate the fast-mode Mach number (M_{f}), corresponding to the fast magnetosonic wave, by

$$M_{\mathrm{f}} = \frac{U_{\mathrm{shock}}}{V_{\mathrm{fms}}}, \tag{A9}$$

with

$$V_{\mathrm{A}} = \frac{B_{\mathrm{up}}}{\sqrt{\mu_0 \rho_{\mathrm{up}}}},\quad c_{\mathrm{s}} = \sqrt{\Gamma \frac{P_{\mathrm{up}}}{\rho_{\mathrm{up}}}},$$
$$V_{\mathrm{fms}} = \sqrt{\frac{1}{2}(V_{\mathrm{A}}^2 + c_{\mathrm{s}}^2) + \sqrt{(V_{\mathrm{A}}^2 + c_{\mathrm{s}}^2)^2 - 4V_{\mathrm{A}}^2 c_{\mathrm{s}}^2 \cos^2\theta_{Bn}}}\,, \tag{A10}$$

where V_{A} denotes the upstream Alfvén speed, and μ_0 is the vacuum permeability; c_{s} denotes the acoustic speed, $\Gamma = 5/3$ is the ratio of specific heats, and P_{up} denotes the upstream ion thermal pressure; V_{fms} denotes the fast magnetosonic speed (e.g., Chapter 69 of L. D. Landau et al. 2013).

ORCID iDs

Weihao Liu https://orcid.org/0000-0002-2873-5688
Igor V. Sokolov https://orcid.org/0000-0002-6118-0469
Lulu Zhao https://orcid.org/0000-0003-3936-5288
Tamas I. Gombosi https://orcid.org/0000-0001-9360-4951
Nishtha Sachdeva https://orcid.org/0000-0001-9114-6133
Xiaohang Chen https://orcid.org/0000-0003-2865-1772
Gábor Tóth https://orcid.org/0000-0001-8459-2100
David Lario https://orcid.org/0000-0002-3176-8704
Ward B. Manchester, IV https://orcid.org/0000-0003-0472-9408
Kathryn Whitman https://orcid.org/0000-0002-3787-1622
Christina M. S. Cohen https://orcid.org/0000-0002-0978-8127
Alessandro Bruno https://orcid.org/0000-0001-5191-1662
M. Leila Mays https://orcid.org/0000-0001-9177-8405
Hazel M. Bain https://orcid.org/0000-0003-2595-3185

References

Abraham-Shrauner, B. 1972, JGR, 77, 736
Altschuler, M. D., & Newkirk, G. 1969, SoPh, 9, 131
Alvarado-Gómez, J. D., Drake, J. J., Cohen, O., Moschou, S. P., & Garraffo, C. 2018, ApJ, 862, 93
Anastasiadis, A., Lario, D., Papaioannou, A., Kouloumvakos, A., & Vourlidas, A. 2019, RSPTA, 377, 20180100
Antiochos, S. K. 2013, ApJ, 772, 72
Antiochos, S. K., DeVore, C., & Klimchuk, J. 1999, ApJ, 510, 485
Aran, A., Sanahuja, B., & Lario, D. 2006, AdSpR, 37, 1240
Armstrong, T. P., Pesses, M. E., & Decker, R. B. 1985, Collisionless Shocks in the Heliosphere: Reviews of Current Research, Vol. 35 (Washington, DC: American Geophysical Union), 271
Axford, W., Leer, E., & Skadron, G. 1977, ICRC (Plovdiv), 15, 132
Bain, H. M., Copeland, K., Onsager, T. G., & Steenburgh, R. A. 2023, SpWea, 21, e2022SW003346
Bale, S. D., Goetz, K., Harvey, P., et al. 2016, SSRv, 204, 49
Band, D., Matteson, J., Ford, L., et al. 1993, ApJ, 413, 281
Bell, A. 1978a, MNRAS, 182, 147
Bell, A. 1978b, MNRAS, 182, 443
Berger, M. J., & Colella, P. 1989, JCoPh, 82, 64
Bertello, L., Pevtsov, A., Petrie, G., & Keys, D. 2014, SoPh, 289, 2419
Blandford, R., & Eichler, D. 1987, PhR, 154, 1
Blandford, R. D., & Ostriker, J. P. 1978, ApJ, 221, L29
Borovikov, D., Sokolov, I., Huang, Z., Roussev, I., & Gombosi, T. 2019, arXiv:1911.10165
Borovikov, D., Sokolov, I., Roussev, I., Taktakishvili, A., & Gombosi, T. 2018, ApJ, 864, 88
Borovikov, D., Sokolov, I. V., Manchester, W. B., Jin, M., & Gombosi, T. I. 2017, JGRA, 122, 7979
Borovikov, D., Sokolov, I. V., & Tóth, G. 2015, JCoPh, 297, 599
Brchnelova, M., Kuźma, B., Perri, B., Lani, A., & Poedts, S. 2022, ApJS, 263, 18
Brüdern, M., Berger, L., Heber, B., et al. 2022, A&A, 663, A89
Brueckner, G. E., Howard, R. A., Koomen, M. J., et al. 1995, SoPh, 162, 357
Bruno, A. 2017, SpWea, 15, 1191
Bruno, A., & Richardson, I. G. 2021, SoPh, 296, 36
Bučík, R. 2020, SSRv, 216, 24
Buzulukova, N., & Tsurutani, B. 2022, FrASS, 9, 1017103
Cane, H., Mewaldt, R., Cohen, C., & Von Rosenvinge, T. 2006, JGRA, 111, A06S90
Chandran, B. D., Dennis, T. J., Quataert, E., & Bale, S. D. 2011, ApJ, 743, 197
Chao, J., & Hsieh, K. 1984, P&SS, 32, 641
Chen, H., Sachdeva, N., Huang, Z., et al. 2025, SpWea, 23, e2024SW004165
Chen, P. 2011, LRSP, 8, 1
Chen, X., Giacalone, J., Guo, F., & Klein, K. G. 2024, ApJ, 965, 61
Chhiber, R., Ruffolo, D., Matthaeus, W. H., et al. 2021, ApJ, 908, 174
Cliver, E. W., Schrijver, C. J., Shibata, K., & Usoskin, I. G. 2022, LRSP, 19, 2
Cohen, C., Mason, G., Mewaldt, R., & Wiedenbeck, M. 2014, ApJ, 793, 35
Cohen, C., Stone, E., Mewaldt, R., et al. 2005, JGRA, 110, A09S16
Dahlin, J. T., DeVore, C. R., & Antiochos, S. K. 2022, ApJ, 941, 79
De Pontieu, B., McIntosh, S., Carlsson, M., et al. 2007, Sci, 318, 1574
de Wit, T. D., Krasnoselskikh, V. V., Bale, S. D., et al. 2020, ApJS, 246, 39
Decker, R. B. 1988, SSRv, 48, 195
Delaunay, B. 1934, Bull. Acad. Science USSR VII: Class. Sci. Mat. Nat., 1, 793, https://www.mathnet.ru/links/95d7c8aa6111426eaf4114db10ced544/im4937.pdf
Desai, M., & Giacalone, J. 2016, LRSP, 13, 3
Ding, L.-G., Li, G., Le, G.-M., Gu, B., & Cao, X.-X. 2015, ApJ, 812, 171
Ding, Z., Wijsen, N., Li, G., & Poedts, S. 2022, A&A, 668, A71
Domingo, V., Fleck, B., & Poland, A. I. 1995, SoPh, 162, 1
Downs, C., Roussev, I. I., van der Holst, B., et al. 2010, ApJ, 712, 1219
Downs, C., Warmuth, A., Long, D. M., et al. 2021, ApJ, 911, 118
Dresing, N., Gómez-Herrero, R., Heber, B., et al. 2014, A&A, 567, A27
Dröge, W., Kartavykh, Y., Klecker, B., & Kovaltsov, G. 2010, ApJ, 709, 912
Drury, L. O. 1983, RPPh, 46, 973
Dumbović, M., Čalogović, J., Vršnak, B., et al. 2018, ApJ, 854, 180
Earl, J. A. 1974, ApJ, 193, 231
Ellison, D. C., Jones, F. C., & Reynolds, S. P. 1990, ApJ, 360, 702
Ellison, D. C., & Ramaty, R. 1985, ApJ, 298, 400
Engelbrecht, N. E. 2019, ApJ, 880, 60
Erdős, G., & Balogh, A. 2005, AdSpR, 35, 625
Fermi, E. 1949, PhRv, 75, 1169
Fisk, L., & Gloeckler, G. 2006, ApJL, 640, L79
Fisk, L., & Gloeckler, G. 2008, ApJ, 686, 1466
Fisk, L., & Schwadron, N. 2001, ApJ, 560, 425
Fox, N., Velli, M., Bale, S., et al. 2016, SSRv, 204, 7
Fulara, A., Chandra, R., Chen, P., et al. 2019, SoPh, 294, 1
Giacalone, J. 2005a, ApJL, 628, L37
Giacalone, J. 2005b, ApJ, 624, 765
Giacalone, J., Jokipii, J., & Mazur, J. 2000, ApJL, 532, L75
Giacalone, J., & Kóta, J. 2007, Solar Dynamics and its Effects on the Heliosphere and Earth (Berlin: Springer), 277
Giacalone, J., & Neugebauer, M. 2008, ApJ, 673, 629
Gibson, S. E., & Low, B. 1998, ApJ, 493, 460
Gieseler, J., Dresing, N., Palmroos, C., et al. 2023, FrASS, 9, 1058810

Gloeckler, G. 2003, in AIP Conf. Proc. 679, Solar Wind Ten (Melville, NY: AIP), 583

Gold, R. E., Krimigis, S. M., Hawkins, S. E., III, et al. 1998, SSRv, 86, 541

Gombosi, T. I. 1998, Physics of the Space Environment (Cambridge: Cambridge Univ. Press), 274

Gombosi, T. I., Chen, Y., Glocer, A., et al. 2021, JSWSC, 11, 42

Gombosi, T. I., De Zeeuw, D. L., Powell, K. G., et al. 2003, Space Plasma Simulation, Vol. 615 (Berlin: Springer), 247

Gombosi, T. I., Powell, K. G., De Zeeuw, D. L., et al. 2004, CSE, 6, 14

Gombosi, T. I., van der Holst, B., Manchester, W. B., & Sokolov, I. V. 2018, LRSP, 15, 1

Gopalswamy, N., Mäkelä, P., Yashiro, S., et al. 2015, Journal of Physics: Conference Series, 642, 012012

Gopalswamy, N., Yashiro, S., Michałek, G., et al. 2002, ApJL, 572, L103

Gopalswamy, N., Yashiro, S., Michalek, G., et al. 2009, EM&P, 104, 295

Guo, J., Wang, B., Whitman, K., et al. 2024, AdSpR, 10.1016/j.asr.2024.03.070

Guo, J., Zeitlin, C., Wimmer-Schweingruber, R. F., et al. 2021, A&ARv, 29, 1

Haggerty, D., Roelof, E., Ho, G., & Gold, R. 2006, AdSpR, 38, 995

Harten, R., & Clark, K. 1995, SSRv, 71, 23

Harvey, J., Hill, F., Hubbard, R., et al. 1996, Sci, 272, 1284

Hayes, A., Vourlidas, A., & Howard, R. 2001, ApJ, 548, 1081

Heras, A., Sanahuja, B., Lario, D., et al. 1995, ApJ, 445, 497

Hill, F. 2018, SpWea, 16, 1488

Hinterreiter, J., Magdalenic, J., Temmer, M., et al. 2019, SoPh, 294, 1

Hollweg, J. V. 1986, JGRA, 91, 4111

Hoppock, I. W., Chandran, B. D., Klein, K. G., Mallet, A., & Verscharen, D. 2018, JPlPh, 84, 905840615

Howard, R. A., Moses, J., Vourlidas, A., et al. 2008, SSRv, 136, 67

Hu, J., Li, G., Ao, X., Zank, G. P., & Verkhoglyadova, O. 2017, JGRA, 122, 10

Huang, Z., Tóth, G., Huang, J., et al. 2024a, ApJL, 965, L1

Huang, Z., Tóth, G., Sachdeva, N., & van der Holst, B. 2024b, ApJ, 965, 1

Hugoniot, H. 1889a, Journal de l'École Polytechnique (French), 57, 1, https://books.google.com/books?id=wccAAAAAYAAJ

Hugoniot, H. 1889b, Journal de l'École Polytechnique (French), 58, 1, https://gallica.bnf.fr/ark:/12148/bpt6k4337130/f11.item

Isenberg, P. A. 1997, JGRA, 102, 4719

Jackson, J. D. 1998, Classical Electrodynamics (3rd ed.; New York: Wiley)

Jian, L., MacNeice, P., Taktakishvili, A., et al. 2015, SpWea, 13, 316

Jin, M., Manchester, W. B., Van Der Holst, B., et al. 2013, ApJ, 773, 50

Jin, M., Manchester, W. B., van der Holst, B., et al. 2017a, ApJ, 834, 172

Jin, M., Manchester, W. B., van der Holst, B., et al. 2017b, ApJ, 834, 173

Jin, M., Nitta, N. V., & Cohen, C. M. 2022, SpWea, 20, e2021SW002894

Jin, M., Schrijver, C., Cheung, M., et al. 2016, ApJ, 820, 16

Jokipii, J. 1982, ApJ, 255, 716

Jokipii, J. 1987, ApJ, 313, 842

Jokipii, J. R. 1966, ApJ, 146, 480

Jones, F. C., & Ellison, D. C. 1991, SSRv, 58, 259

Joshi, B., Kushwaha, U., Veronig, A. M., et al. 2016, ApJ, 834, 42

Kahler, S., Hildner, E., & Van Hollebeke, M. 1978, SoPh, 57, 429

Kahler, S., & Ling, A. 2019, ApJ, 872, 89

Kahler, S., Sheeley, N., Jr., Howard, R., et al. 1984, JGRA, 89, 9683

Kaiser, M. L., Kucera, T., Davila, J., et al. 2008, SSRv, 136, 5

Kasper, J. C., Abiad, R., Austin, G., et al. 2016, SSRv, 204, 131

Kataoka, R., Ebisuzaki, T., Kusano, K., et al. 2009, JGRA, 114, A10102

Kecskeméty, K., Daibog, E., Logachev, Y. I., & Kóta, J. 2009, JGRA, 114, A06102

Kennis, S., Perri, B., & Poedts, S. 2024, A&A, 691, A257

Kilpua, E. K., Lugaz, N., Mays, M. L., & Temmer, M. 2019, SpWea, 17, 498

King, J., & Papitashvili, N. 2005, JGRA, 110, A02104

Kleimann, J., Dialynas, K., Fraternale, F., et al. 2022, SSRv, 218, 36

Klein, K.-L., & Dalla, S. 2017, SSRv, 212, 1107

Kolmogorov, A. 1941, DoSSR, 30, 301

Kong, X., Guo, F., Chen, Y., & Giacalone, J. 2019, ApJ, 883, 49

Kóta, J. 1997, ICRC (Durban), 25, 213

Kóta, J. 2000, JGRA, 105, 2403

Kóta, J., & Jokipii, J. 2004, in AIP Conf. Proc. 719, Physics of the Outer Heliosphere (Melville, NY: AIP), 272

Kóta, J., Manchester, W. B., Jokipii, J., De Zeeuw, D., & Gombosi, T. 2005, in AIP Conf. Proc. 781, The Physics of Collisionless Shocks (Melville, NY: AIP), 201

Kouloumvakos, A., Rouillard, A. P., Wu, Y., et al. 2019, ApJ, 876, 80

Krivodonova, L., & Smirnov, A. 2021, arXiv:2110.00067

Krymskii, G. 1977, DoSSR, 234, 1306

Kühl, P., & Heber, B. 2019, SpWea, 17, 84

Kwon, R.-Y., & Vourlidas, A. 2017, ApJ, 836, 246

Kwon, R.-Y., Zhang, J., & Olmedo, O. 2014, ApJ, 794, 148

Laitinen, T., Dalla, S., & Marsh, M. 2013, ApJL, 773, L29

Laitinen, T., Effenberger, F., Kopp, A., & Dalla, S. 2018, JSWSC, 8, A13

Laitinen, T., Kopp, A., Effenberger, F., Dalla, S., & Marsh, M. 2016, A&A, 591, A18

Landau, L., & Lifshitz, E. 1960, Course of Theoretical Physics: Mechanics, Vol. 1 (Oxford: Pergamon),

Landau, L. D., Bell, J. S., Kearsley, M., et al. 2013, Electrodynamics of Continuous Media, Vol. 8 (Amsterdam: Elsevier)

Landau, L. D., & Lifshitz, E. M. 1987, Fluid Mechanics, Vol. 6 (Amsterdam: Elsevier),

Lario, D., Balmaceda, L. A., Gómez-Herrero, R., et al. 2024, ApJ, 975, 84

Lario, D., Berger, L., Decker, R., et al. 2019, AJ, 158, 12

Lario, D., Berger, L., Wilson, L. B., III, et al. 2018, Journal of Physics: Conference Series, 1100, 012014

Lario, D., Kallenrode, M.-B., Decker, R., et al. 2006, ApJ, 653, 1531

Lario, D., Raouafi, N., Kwon, R.-Y., et al. 2014, ApJ, 797, 8

Lario, D., Sanahuja, B., & Heras, A. 1998, ApJ, 509, 415

Lee, C., Luhmann, J., Hoeksema, J., et al. 2011, SoPh, 269, 367

Lee, D.-T., & Schachter, B. J. 1980, International Journal of Computer & Information Sciences, 9, 219

Lee, M. A. 1982, JGRA, 87, 5063

Lee, M. A. 1983, JGRA, 88, 6109

Lee, M. A., Mewaldt, R., & Giacalone, J. 2012, SSRv, 173, 247

Lemen, J. R., Title, A. M., Akin, D. J., et al. 2012, SoPh, 275, 17

Lepping, R., & Argentiero, P. 1971, JGR, 76, 4349

Li, G., & Lee, M. A. 2015, ApJ, 810, 82

Li, G., Moore, R., Mewaldt, R., Zhao, L., & Labrador, A. 2012, SSRv, 171, 141

Li, G., & Zank, G. 2005, GeoRL, 32, L02101

Li, G., Zank, G., & Rice, W. 2003, JGRA, 108, 1082

Li, G., Zank, G., Verkhoglyadova, O., et al. 2009, ApJ, 702, 998

Linker, J. A., Caplan, R. M., Schwadron, N., et al. 2019, Journal of Physics: Conference Series, 1225, 012007

Liouville, J. 1838, Journal de Mathématiques pures et Appliquées, 3, 342

Liu, X., Liu, W., Manchester, W. B., et al. 2025, arXiv:2503.10974

Lugaz, N., Farrugia, C. J., Manchester, W. B., & Schwadron, N. 2013, ApJ, 778, 20

Lugaz, N., Manchester, W. B., & Gombosi, T. I. 2005a, ApJ, 627, 1019

Lugaz, N., Manchester, W. B., & Gombosi, T. I. 2005b, ApJ, 634, 651

Lugaz, N., Manchester, W. B., Roussev, I. I., Tóth, G., & Gombosi, T. I. 2007, ApJ, 659, 788

Luhmann, J., Ledvina, S., Krauss-Varban, D., Odstrcil, D., & Riley, P. 2007, AdSpR, 40, 295

Luhmann, J. G., Gopalswamy, N., Jian, L., & Lugaz, N. 2020, SoPh, 295, 61

MacNamara, S., & Strang, G. 2016, Splitting Methods in Communication, Imaging, Science, and Engineering (Berlin: Springer), 95

Maguire, C. A., Carley, E. P., McCauley, J., & Gallagher, P. T. 2020, A&A, 633, A56

Malandraki, O., Marsden, R., Lario, D., et al. 2009, ApJ, 704, 469

Manchester, W. B., Gombosi, T., DeZeeuw, D., & Fan, Y. 2004, ApJ, 610, 588

Manchester, W. B., Gombosi, T., De Zeeuw, D., et al. 2005, ApJ, 622, 1225

Manchester, W. B., Gombosi, T. I., Roussev, I., et al. 2004a, JGRA, 109, A01102

Manchester, W. B., Gombosi, T. I., Roussev, I., et al. 2004b, JGRA, 109, A02107

Manchester, W. B., Kilpua, E. K., Liu, Y. D., et al. 2017, SSRv, 212, 1159

Manchester, W. B., Kozyra, J., Lepri, S., & Lavraud, B. 2014a, JGRA, 119, 5449

Manchester, W. B., Ridley, A., Gombosi, T., & DeZeeuw, D. 2006, AdSpR, 38, 253

Manchester, W. B., van der Holst, B., & Lavraud, B. 2014b, PPCF, 56, 064006

Manchester, W. B., Vourlidas, A., Tóth, G., et al. 2008, ApJ, 684, 1448

Marhavilas, P., Malandraki, O., & Anagnostopoulos, G. 2015, P&SS, 117, 192

Mason, G. 2007, SSRv, 130, 231

Matthaeus, W. H., Zank, G. P., Smith, C. W., & Oughton, S. 1999, PhRvL, 82, 3444

Mays, M., Taktakishvili, A., Pulkkinen, A., et al. 2015, SoPh, 290, 1775

Melrose, D., & Pope, M. 1993, PASA, 10, 222

Meng, X., Van der Holst, B., Tóth, G., & Gombosi, T. 2015, MNRAS, 454, 3697

Menzel, W. P., & Purdom, J. F. 1994, BAMS, 75, 757

Mewaldt, R., Cohen, C., Labrador, A., et al. 2005, JGRA, 110, A09S18

Mewaldt, R. A., Cohen, C., Cook, W., et al. 2008, SSRv, 136, 285

Mikić, Z., & Lee, M. 2006, SSRv, 123, 57

Millward, G., Biesecker, D., Pizzo, V., & De Koning, C. 2013, SpWea, 11, 57
Miroshnichenko, L. I. 2018, JSWSC, 8, A52
Miteva, R., Samwel, S., & Costa-Duarte, M. 2018, JASTP, 180, 26
Miteva, R., Samwel, S. W., Zabunov, S., & Dechev, M. 2020, BlgAJ, 33, 99
Morgado, B., Maia, D. J. F., Lanzerotti, L., Gonçalves, P., & Patterson, J. D. 2015, A&A, 577, A61
Morgan, H., Habbal, S. R., & Woo, R. 2006, SoPh, 236, 263
Moussas, X., Quenby, J., Theodossiou-Ekaterinidi, Z., et al. 1992, SoPh, 140, 161
Müller-Mellin, R., Böttcher, S., Falenski, J., et al. 2008, SSRv, 136, 363
Ng, C., & Reames, D. 1994, ApJ, 424, 1032
Ng, C., Reames, D., & Tylka, A. 2003, ApJ, 591, 461
Nikolić, L. 2019, SpWea, 17, 1293
Nitta, N. V., Reames, D. V., DeRosa, M. L., et al. 2006, ApJ, 650, 438
Northrop, T. G. 1963, RvGSP, 1, 283
Onsager, T., Grubb, R., Kunches, J., et al. 1996, Proc. SPIE, 2812, 281
Ontiveros, V., & Vourlidas, A. 2009, ApJ, 693, 267
Oran, R., van der Holst, B., Landi, E., et al. 2013, ApJ, 778, 176
Paassilta, M., Papaioannou, A., Dresing, N., et al. 2018, SoPh, 293, 1
Palmerio, E., Kilpua, E. K., Möstl, C., et al. 2018, SpWea, 16, 442
Palmerio, E., Luhmann, J. G., Mays, M. L., et al. 2024, JSWSC, 14, 3
Pan, H., Gou, T., & Liu, R. 2022, ApJ, 937, 77
Park, J., Innes, D., Bucik, R., Moon, Y.-J., & Kahler, S. 2015, ApJ, 808, 3
Park, J., Moon, Y.-J., & Lee, H. 2017, ApJ, 844, 17
Parker, E. N. 1958, ApJ, 128, 664
Parker, E. N. 1965, P&SS, 13, 9
Pesnell, W. D., Thompson, B. J., & Chamberlin, P. C. 2012, SoPh, 275, 3
Petrie, G. J. 2015, LRSP, 12, 1
Petrosian, V. 2012, SSRv, 173, 535
Pierrard, V., & Lazar, M. 2010, SoPh, 267, 153
Pitňa, A., Šafránková, J., Němeček, Z., Ďurovcová, T., & Kis, A. 2021, FrP, 8, 626768
Plotnikov, I., Rouillard, A. P., & Share, G. H. 2017, A&A, 608, A43
Powell, K. G., Roe, P. L., Linde, T. J., Gombosi, T. I., & De Zeeuw, D. L. 1999, JCoPh, 154, 284
Prinsloo, P., Strauss, R., & Le Roux, J. 2019, ApJ, 878, 144
Pucci, F., Malara, F., Perri, S., et al. 2016, MNRAS, 459, 3395
Qin, G., Zhang, M., Dwyer, J. R., Rassoul, H. K., & Mason, G. M. 2005, ApJ, 627, 562
Rankine, W. J. M. 1870, Philosophical Transactions of the Royal Society of London, 160, 277
Reames, D. V. 1999, SSRv, 90, 413
Reames, D. V. 2013, SSRv, 175, 53
Reames, D. V. 2021, Solar Energetic Particles A Modern Primer on Understanding Sources, Acceleration and Propagation (Berlin: Springer)
Reiss, M. A., Arge, C. N., Henney, C. J., et al. 2023, AdSpR
Richardson, I., Mays, M., & Thompson, B. 2018, SpWea, 16, 1862
Richardson, I., Von Rosenvinge, T., Cane, H., et al. 2014, Coronal Magnetometry (Berlin: Springer), 437
Robbrecht, E., Berghmans, D., & Van der Linden, R. 2009, ApJ, 691, 1222
Roelof, E. 1969, Lectures in High-Energy Astrophysics NSSDC-ID-66-049A-01-PM, NASA 111, https://ntrs.nasa.gov/citations/19690020281
Rouillard, A., Odstrc, D., Sheeley, N., et al. 2011, ApJ, 735, 7
Rouillard, A. P., Plotnikov, I., Pinto, R. F., et al. 2016, ApJ, 833, 45
Roussev, I. I., Forbes, T. G., Gombosi, T. I., et al. 2003, ApJL, 588, L45
Sachdeva, N., Manchester, W. B., Sokolov, I., et al. 2023, ApJ, 952, 117
Sachdeva, N., Tóth, G., Manchester, W. B., et al. 2021, ApJ, 923, 176
Sachdeva, N., van Der Holst, B., Manchester, W. B., et al. 2019, ApJ, 887, 83
Schatten, K. H., Wilcox, J. M., & Ness, N. F. 1969, SoPh, 6, 442
Sellers, F. B., & Hanser, F. A. 1996, Proc. SPIE, 2812, 353
Shalchi, A. 2019, AdSpR, 64, 2426
Shalchi, A. 2020, SSRv, 216, 23
Shalchi, A. 2021, PhPl, 28, 120501
Shen, F., Feng, X., Wu, S., Xiang, C., & Song, W. 2011, JGRA, 116, A04102
Shi, T., Manchester, W. B., Landi, E., et al. 2022, ApJ, 928, 34
Shiota, D., & Kataoka, R. 2016, SpWea, 14, 56
Shoda, M., Chandran, B. D., & Cranmer, S. R. 2021, ApJ, 915, 52
Sime, D., & Hundhausen, A. 1987, JGRA, 92, 1049
Skilling, J. 1971, ApJ, 170, 265
Smith, Z., & Dryer, M. 1990, SoPh, 129, 387
Sokolov, I. V., & Gombosi, T. I. 2023, ApJ, 955, 126
Sokolov, I. V., Powell, K. G., Gombosi, T. I., & Roussev, I. I. 2006a, JCoPh, 220, 1
Sokolov, I. V., Roussev, I., Fisk, L., et al. 2006b, ApJ, 642, L81
Sokolov, I. V., Roussev, I., Gombosi, T., et al. 2004, ApJL, 616, L171
Sokolov, I. V., Roussev, I. I., Skender, M., Gombosi, T. I., & Usmanov, A. V. 2009, ApJ, 696, 261
Sokolov, I. V., Sun, H., Tóth, G., et al. 2019, arXiv:1910.12636v1
Sokolov, I. V., Sun, H., Tóth, G., et al. 2023, JCoPh, 476, 111923
Sokolov, I. V., van der Holst, B., Manchester, W. B., et al. 2021, ApJ, 908, 172
Sokolov, I. V., van der Holst, B., Oran, R., et al. 2013, ApJ, 764, 23
Sokolov, I. V., Zhao, L., & Gombosi, T. I. 2022, ApJ, 926, 102
Stone, E. C., Frandsen, A., Mewaldt, R., et al. 1998, SSRv, 86, 1
Strang, G. 1968, SJNA, 5, 506
Strauss, R., & Fichtner, H. 2015, ApJ, 801, 29
Temmer, M., Preiss, S., & Veronig, A. 2009, SoPh, 256, 183
Temmer, M., Scolini, C., Richardson, I. G., et al. 2023, AdSpR, 10.1016/j.asr.2023.07.003
Thompson, W. T., Davila, J. M., Fisher, R. R., et al. 2003, Proc. SPIE, 4853, 1
Titov, V. S., & Démoulin, P. 1999, A&A, 351, 707
Titov, V. S., Downs, C., Török, T., & Linker, J. A. 2022, ApJ, 936, 121
Titov, V. S., Török, T., Mikic, Z., & Linker, J. A. 2014, ApJ, 790, 163
Török, T., Downs, C., Linker, J. A., et al. 2018, ApJ, 856, 75
Torsti, J., Valtonen, E., Lumme, M., et al. 1995, SoPh, 162, 505
Tóth, G. 2023, JCoPh, 494, 112534
Tóth, G., Sokolov, I. V., Gombosi, T. I., et al. 2005, JGRA, 110, A12226
Tóth, G., van der Holst, B., & Huang, Z. 2011, ApJ, 732, 102
Tóth, G., van der Holst, B., Sokolov, I. V., et al. 2012, JCoPh, 231, 870
Treumann, R. 2009, A&ARv, 17, 409
Tsurutani, B. T., Sen, A., Hajra, R., et al. 2024, JGRA, 129, e2024JA032622
Tylka, A., Cohen, C., Dietrich, W., et al. 2005, ApJ, 625, 474
Vainio, R. 2003, A&A, 406, 735
Valtonen, E., Peltonen, J., Peltonen, P., et al. 1997, NIMPA, 391, 249
van den Berg, J., Strauss, D. T., & Effenberger, F. 2020, SSRv, 216, 146
van der Holst, B., Huang, J., Sachdeva, N., et al. 2022, ApJ, 925, 146
van der Holst, B., Manchester, W. B., Frazin, R., et al. 2010, ApJ, 725, 1373
van der Holst, B., Manchester, W. B., Klein, K., & Kasper, J. 2019, ApJL, 872, L18
van der Holst, B., Manchester, W. B., Sokolov, I., et al. 2009, ApJ, 693, 1178
van der Holst, B., Sokolov, I. V., Meng, X., et al. 2014, ApJ, 782, 81
van der Holst, B., Tóth, G., Sokolov, I. V., et al. 2011, ApJS, 194, 23
Vemareddy, P., & Mishra, W. 2015, ApJ, 814, 59
Verkhoglyadova, O. P., Zank, G. P., & Li, G. 2015, PhR, 557, 1
Von Rosenvinge, T., Reames, D., Baker, R., et al. 2008, The STEREO Mission (Berlin: Springer), 391
Vourlidas, A., Wu, S., Wang, A., Subramanian, P., & Howard, R. 2003, ApJ, 598, 1392
Wang, Y., & Guo, J. 2024, A&A, 691, A54
Wang, Y., & Qin, G. 2015, ApJ, 806, 252
Webb, D. F., & Howard, T. A. 2012, LRSP, 9, 1
Whang, Y., Zhou, J., Lepping, R., & Ogilvie, K. 1996, GeoRL, 23, 1239
Whitman, K., Egeland, R., Richardson, I. G., et al. 2023, AdSpR, 72, 5161
Wijsen, N., Aran, A., Pomoell, J., & Poedts, S. 2019, A&A, 622, A28
Wijsen, N., Li, G., Ding, Z., et al. 2023, JGRA, 128, e2022JA031203
Wraback, E., Hoffmann, A., Manchester, W. B, et al. 2024, ApJ, 962, 182
Wuelser, J.-P., Lemen, J. R., Tarbell, T. D., et al. 2004, Proc. SPIE, 5171, 111
Xie, H., St. Cyr, O., Mäkelä, P., & Gopalswamy, N. 2019, JGRA, 124, 6384
Yashiro, S., Gopalswamy, N., Michalek, G., et al. 2004, JGRA, 109, A07105
Young, M. A., Schwadron, N. A., Gorby, M., et al. 2021, ApJ, 909, 160
Yu, F., Kong, X., Guo, F., et al. 2022, ApJL, 925, L13
Zakharov, V. E., L'vov, V. S., & Falkovich, G. 2012, Kolmogorov Spectra of Turbulence I Wave Turbulence (Berlin: Springer)
Zank, G., Le Roux, J., Webb, G., Dosch, A., & Khabarova, O. 2014, ApJ, 797, 28
Zank, G., Li, G., & Verkhoglyadova, O. 2007, SSRv, 130, 255
Zank, G., Rice, W., & Wu, C. 2000, JGRA, 105, 25079
Zhang, M., Cheng, L., Zhang, J., et al. 2023, ApJS, 266, 35
Zhang, M., Qin, G., & Rassoul, H. 2009, ApJ, 692, 109
Zhang, M., & Zhao, L. 2017, ApJ, 846, 107
Zhao, L., Li, G., Zhang, M., et al. 2019, ApJ, 878, 107
Zhao, L., Sokolov, I., Gombosi, T., et al. 2024, SpWea, 22, e2023SW003729
Zhao, L., Zhang, M., & Rassoul, H. K. 2016, ApJ, 821, 62
Zhao, L., Zhang, M., & Rassoul, H. K. 2017, ApJ, 836, 31
Zheng, Y., Jun, I., Tu, W., et al. 2024, AdSpR, 10.1016/j.asr.2024.05.017
Zhuang, B., Lugaz, N., Gou, T., & Ding, L. 2021, ApJ, 921, 6
Zucca, P., Morosan, D. E., Rouillard, A., et al. 2018, A&A, 615, A89